










Seismic reliability of Italian code-conforming bridges

Paolo Franchin¹  | Georgios Baltzopoulos²  | Fabio Biondini³ | Luigi Callisto¹  |
 Luca Capacci³  | Sandro Carbonari⁴ | Donatello Cardone⁵  |
 Andrea Dall'Asta⁶  | Amedeo Flora⁵ | Davide Noè Gorini¹  | Andrea Marchi¹  |
 Fabrizio Noto⁷ | Giuseppe Perrone⁵ | Iunio Iervolino² 

¹Dipartimento, di Ingegneria Strutturale e Geotecnica, Università di Roma La Sapienza, Rome, Italy

²Dipartimento di Strutture per l'Ingegneria e l'Architettura, Università degli Studi di Napoli Federico II, Naples, Italy

³Dipartimento di Ingegneria Civile e Ambientale, Politecnico di Milano, Milan, Italy

⁴Dipartimento di Progettazione e Costruzione dell'Ambiente, Università di Camerino, Ascoli Piceno, Italy

⁵Scuola di Ingegneria, Università della Basilicata, Potenza, Italy

⁶Scuola di Architettura e Design, Università di Camerino, Ascoli Piceno, Italy

⁷METIS Engineering, Rome, Italy

Correspondence

Paolo Franchin, Dipartimento di Ingegneria Strutturale e Geotecnica, Università di Roma La Sapienza, Rome, Italy.
 Email: paolo.franchin@uniroma1.it

Abstract

Seismic reliability assessment of selected bridge structures code-conforming with respect to the current Italian practice is carried out. Two viaducts, tall and shallow, and two highway overpasses, with traditional seat-type or integral abutments, are considered. Each structure is ideally placed at three reference sites, that is, Milan, Naples and L'Aquila, characterised by low, moderate and high seismic hazard, respectively. At each site, a soil profile representative of typical local conditions is defined for foundation design, site response analysis and soil-structure interaction modelling. Probabilistic seismic hazard is used in conjunction with multiple-stripe non-linear dynamic analysis, featuring conditional-spectrum compatible ground motions, to establish the failure rate with respect to two purposely defined and functionality-related performance levels. It is confirmed the decreasing seismic reliability with increasing design seismic action, already observed for other structural types, and it is shown that integral abutment overpasses tend to be more reliable than traditional ones, even seismically isolated ones. The results are of larger interest given the closeness of the Italian code to the Eurocode.

KEYWORDS

friction pendulum slider, hazard-consistent motions, high damping rubber bearing, integral abutment, soil structure interaction

1 | INTRODUCTION

This paper reports about the seismic reliability assessment of typical code-conforming Italian bridge structures.¹ Four archetype bridges were selected: two viaducts, tall and shallow and two overpasses, with traditional seat-type or integral abutments. Each archetype was placed and designed according to the current Italian code² at three sites, that is, Milan, Naples and L'Aquila, that can be considered as characterised by low, moderate and high seismicity, respectively. At each site, a soil profile representative of typical local conditions was defined, for the purpose of foundation design. Seismic reliability was then assessed in terms of failure rate with respect to two purposely defined and functionality-related performance levels. The failure rate was calculated by integrating structural seismic fragility and each site's hazard. The former

This is an open access article under the terms of the [Creative Commons Attribution-NonCommercial](https://creativecommons.org/licenses/by-nc/4.0/) License, which permits use, distribution and reproduction in any medium, provided the original work is properly cited and is not used for commercial purposes.

© 2023 The Authors. *Earthquake Engineering & Structural Dynamics* published by John Wiley & Sons Ltd.

NOVELTY

- Italian bridges representative of current code-conforming highway structures, including both viaducts and highway overpasses, are analysed.
- The archetype structures include traditional design exploiting ductility, seismic isolation with both elastomeric and sliding devices and integral abutment bridges.
- Probabilistic seismic performance assessment is performed with hazard curves from site-specific PSHA and fragility curves from multiple stripe analysis of state-of-the-art models with hazard-consistent ground motions.
- Models include soil-foundation-structure interaction.
- Mean annual failure rate is calculated with reference to two functionality-related performance levels.
- Values of the rates confirm the dependence of reliability on-site seismicity, already observed and explained with reference to buildings.
- Values are compared to target reliability under discussion in the context of the revision of the structural Eurocodes and found to be in general satisfactory.
- Significant inter-typology differences are also observed.

was evaluated by means of probabilistic seismic hazard analysis (PSHA),³ while the latter based on response samples obtained by means of multiple-stripe non-linear dynamic analysis (MSA).⁴ Site-response analysis (SRA)⁵ was performed to amplify all input ground motions, using a model of the already cited soil profiles. Soil-foundation-structure interaction (SFSI)⁶ was accounted for in the non-linear dynamic analysis.

Similar studies of a large portfolio of structures or of a smaller set of archetypal structures have been carried out in the past. Haselton et al.⁷ and Liel et al.⁸ determined collapse safety of archetypal ductile (code-compliant) and non-ductile reinforced concrete (RC) building frames, respectively, using two-dimensional (2D) models. Similarly, Iervolino et al.^{9,10} focused on safety of archetypal buildings in Italy, compliant to different codes enforced over the course of the last century, and employing three-dimensional (3D) models developed for each structural typology, for instance for RC buildings Ricci et al.,¹¹ De Risi et al.¹² and Di Domenico et al.¹³

Regarding bridges, as early as 1997, Basoz and Kiremidjian¹⁴ performed risk assessment via non-linear dynamic analysis. Nielson and DesRoches,¹⁵ Moschonas et al.¹⁶ and Avşar et al.¹⁷ all provided seismic fragility curves for typical bridges in the Central and Southeastern United States, Greece and Turkey, respectively. Finally, Borzi et al.¹⁸ also calculated safety for two performance levels (light damage and collapse) and with 3D models, with reference to a large database of real Italian bridges, but these were non-conforming older bridges, and no consideration was given at the time to SFSI.

The paper is organised as follows. Section 2 presents hazard and ground motion selection. Section 3 presents the four selected bridges. Section 4 illustrates the models adopted for the assessment, from the geotechnical properties of the sites and site response analysis to the inelastic modelling for all components, from the deck to the soil-foundation system. Section 5 presents the adopted performance criteria. Sections 6 and 7 illustrate sample results of the non-linear dynamic analyses and summarise the results in terms of reliability. Section 8 draws conclusions.

2 | SITES, HAZARD AND GROUND MOTIONS

Three Italian sites were used to represent low, moderate and high seismicity: Milan, Naples and L'Aquila (Figure 1). Site-specific PSHA, consistent with that underlying the current design provisions, was carried out for all spectral ordinates of interest in the largest context of the RINTC project.¹⁰ This produced hazard curves, later integrated with fragility curves to yield annual rates, and hazard disaggregation, used to select recorded ground motions which are hazard consistent in terms of spectral shape and of the main parameters of the most likely causative events: earthquake magnitude, M , and source-to-site distance, R . The actual selection procedure¹⁹ is deemed an enhancement of the *Conditional Spectrum* (CS) method²⁰ and, for each site, can be summarised as follows:

- Disaggregate hazard,²¹ conditional on the spectral acceleration at the conditioning vibration period T_c (see later, Table 1), $S_a(T_c) = sa_i$, where sa_i corresponds to each one of the considered ten values with exceedance return periods

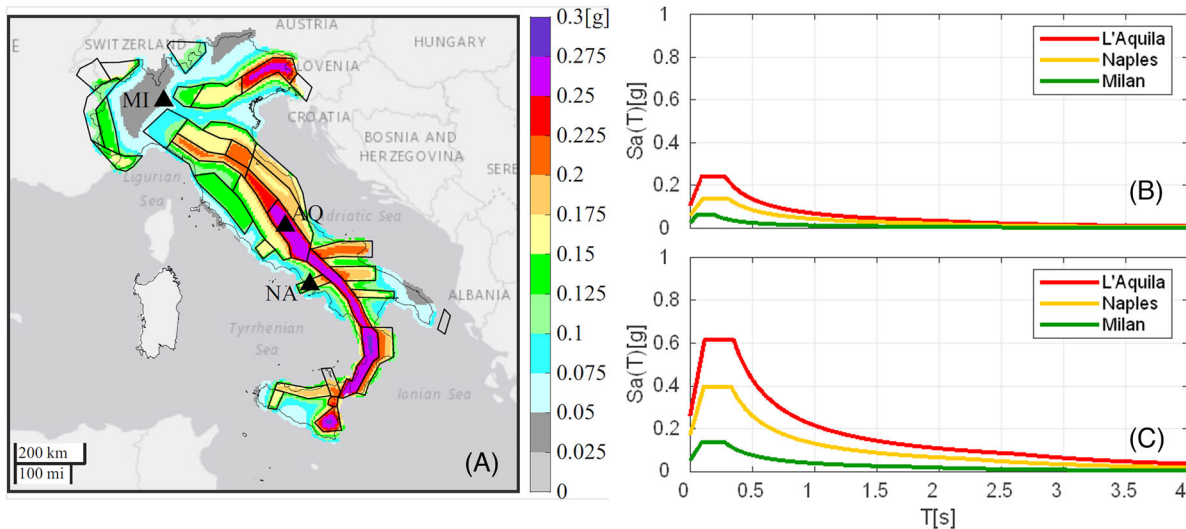


FIGURE 1 Peak ground acceleration (soil A) with 10% probability of exceedance in 50 years in Italy and the location of the three sites (A), uniform hazard spectra (soil A) at the three sites with 63%/50 (B) and 10%/50 (C) probability of exceedance, respectively. Panel (A) shows also the thirty-six seismic area sources of the source model at the basis of the building code currently enforced in Italy.

TABLE 1 Fundamental periods in the longitudinal (T_X) and transevsral (T_Y) directions and conditioning period (T_c) used in ground motion record selection. Bold numbers indicate the ten distinct selections (period and site).

Site Bridge	Milan			Naples			L'Aquila		
	T_X (s)	T_Y (s)	T_c (s)	T_X (s)	T_Y (s)	T_c (s)	T_X (s)	T_Y (s)	T_c (s)
TV	1.67	0.88	1.50	1.18	0.88	1.00	1.32	0.88	1.00
SV	0.82	0.27	0.50	2.27	2.23	2.00	2.73	2.70	3.00
TO	0.78	0.25	0.50	0.78	0.25	0.50	–	–	–
HDRB	–	–	–	1.58	1.58	1.50	1.48	1.48	1.50
FPS	–	–	–	1.90	1.90	2.00	2.30	2.30	2.00
IAB	0.55	0.35	0.50	0.46	0.29	0.50	0.27	0.28	0.50

$T_R = \{10, 50, 100, 250, 500, 1000, 2500, 5000, 10,000, 100,000\}$ years, denoted in the following as intensity measure levels (IML) from 1 to 10;

- Determine, for each IML, the corresponding CS distribution;¹
- Sample, for each IML, twenty response spectra from the corresponding CS distribution;
- Select, for each IML, the twenty real ground motion records with spectra closest to the simulated ones;
- Post-process, for each IML, the selected set, eventually replacing the records that are not disaggregation-consistent with other spectrally equivalent ground motions with desired M and R from disaggregation.

Hence, the selection procedure delivered two hundred pairs of records for each intensity measure (IM), twenty records for each one of the ten stripes.²² The procedure was applied checking compatibility of horizontal components with horizontal target spectra, while the vertical components are simply those recorded with the selected motions. Finally, note that ground motions were selected as outcrop (soil category A^2), since they were later subjected to site response analysis prior to use in MSA (see 0).

¹To compute the CS distribution a GMPE is required. For consistency with PSHA, the one from Ambraseys et al.²³ has been used, which considers, as the IM , the maximum spectral acceleration between the two horizontal components. However, it is limited to spectral ordinates up to $Sa(T = 2s)$; therefore, when the vibration period of the conditioning spectral acceleration was larger than $2s$ a different GMPE²⁴ was considered. It considers, as the IM , the geometric mean of the two horizontal components so, for consistency, when the vibration period of the conditioning spectral acceleration is greater than $2s$ the CS matching was performed using the latter as IM .

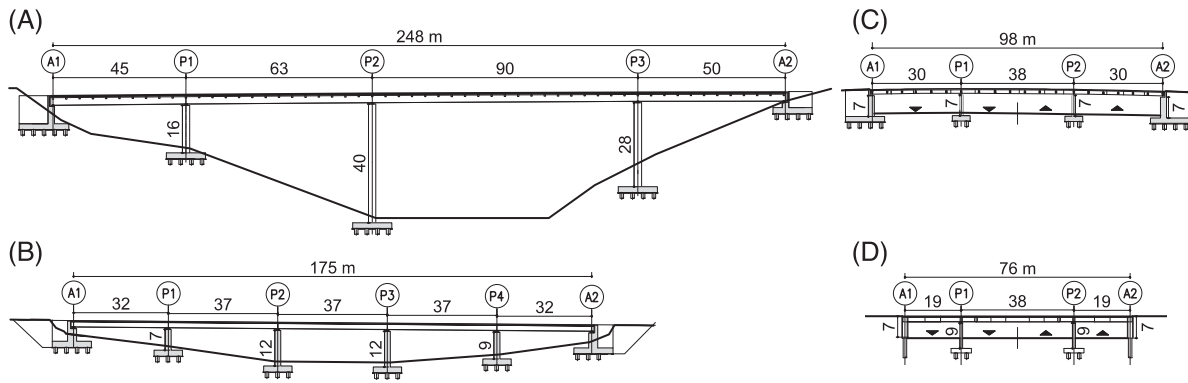


FIGURE 2 Archetype bridges: (A) tall viaduct, (B) shallow viaduct, (C) traditional overpass, (D) integral abutment overpass. Total and partial measures in meters.

3 | ARCHETYPE BRIDGES

The archetype bridges are schematically shown in Figure 2. They were designed according to Italian technical provisions currently in force.² Analysis for the purpose of design was carried out with the Sap2000 software²⁵ (SAP2000, see Franchin et al.²² for details on the adopted design procedures). For all archetype bridges, current modelling practice was taken as a reference and 3D models were used. All superstructures are continuous over the supports. Off-the-shelf bearings and devices accommodating seismic demand were used throughout.^{26,27}

All bridge substructures rest on pile foundations. The latter were designed with reference to ultimate limit states (LS) under static and seismic conditions. The resulting foundations are composed of RC piles varying in number from 15 to 40, with diameter D in the range 0.8–1.2 m, spacing not less than $3D$ and a maximum length of 54 m in the case of the tall viaduct in L'Aquila.

In terms of design LS, the design seismic action for all structural members, except for anti-seismic devices, is characterised by a probability of exceedance of 10% in 100 years ($T_R = 949$ years). For this intensity, the LS is that of *life safety* according to the Italian code (*significant damage* according to Eurocode terminology²⁸).

The 'tall viaduct' (TV) is a three-lane four-span highway bridge composed of a continuous two-girder composite steel-concrete deck with a total span of 248 m, supported by RC piers labelled P1, P2 and P3, with a height of 16, 40 and 28 m, respectively. Piers are two-column bents, with hollow rectangular cross-section, connected by a coupling pier cap at their top. Given the height and flexibility of P2 and P3, fixed bearings are used over such piers to restrain their top displacement, whilst the deck rests through longitudinal flat sliders over the shorter P1. Seismic expansion joints are provided at the seat-type RC abutments to accommodate the longitudinal deck translation. Nonlinear viscous dampers are placed at the right abutment to limit displacements only at the more seismic Naples and L'Aquila sites. Figure 3 shows cross-section dimensions, the configuration of bearings and (so-called) anti-seismic devices, and a sample layout of pier reinforcement. Concrete, reinforcement and structural steel classes are C32/40, B450C and S355W, respectively. Note that damper forces have been considered in the design of the abutment. According to Italian practice, dampers are placed on one abutment only as long as the required forces are not excessive.

The shallow viaduct (SV) has a continuous two-girder composite deck, supported by four RC piers with height in the range 7–12 m. Longitudinal flat sliders are used overall piers in Milan, and nonlinear viscous dampers, connected to the deck through the steel girders, are placed at the right abutment. Double curvature surface sliders (DCSS) are adopted for the higher seismicity sites of Naples and L'Aquila, with larger radius at the latter site. Figure 4 shows cross-section dimensions, the configuration of bearings and devices, and a sample layout of pier reinforcement. Concrete, reinforcement and structural steel classes are C30/37, B450C and S355W, respectively. For the purpose of design of both TVs and SVs, equivalent linear properties with iteration on the maximum displacement, followed by non-linear dynamic analysis verification was used.

The highway overpass with seat-type abutments is illustrated in Figure 5. It is composed of three continuous straight spans (30 + 38 + 30 m) with composite deck, supported over two 7-m high RC piers with compact cross-section. The steel deck is 12 m wide and steel beams are of the Welded Wide Flange type. In terms of bearings, fixed and uni/multi-directional mobile bearings are considered in Milan (traditional overpass configuration, TO) and base-isolation, with both

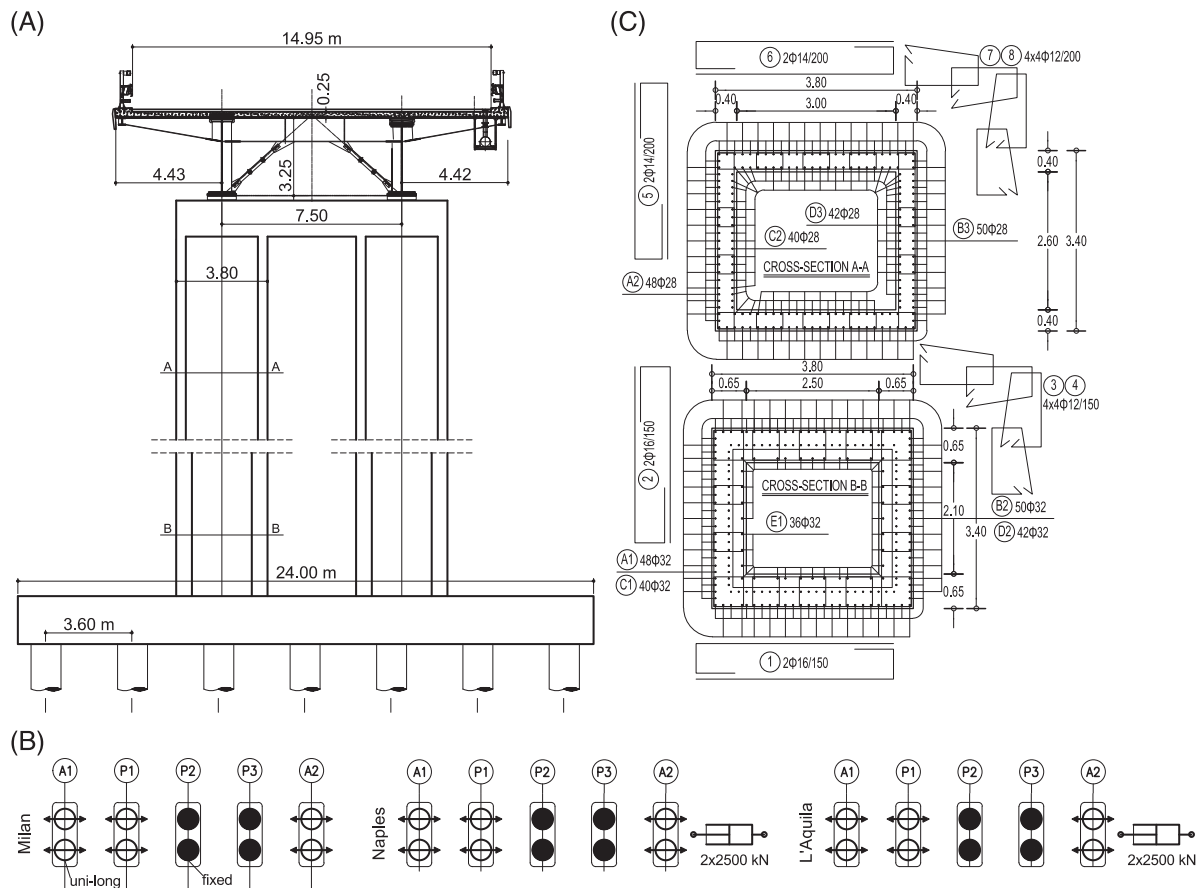


FIGURE 3 Tall viaduct: deck cross-section (A), bearings layout (B) and pier P2 cross-section with reinforcement for L'Aquila (C).

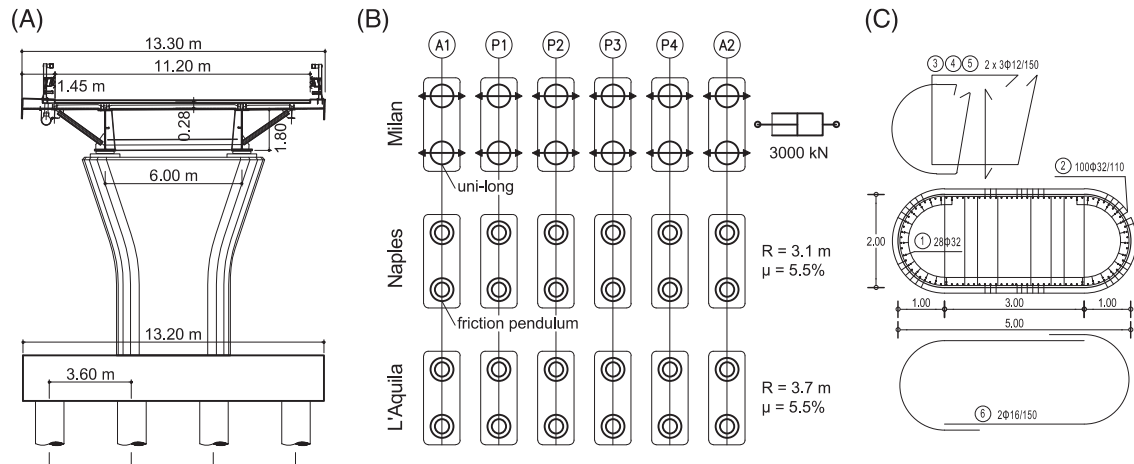


FIGURE 4 Shallow viaduct: deck cross-section (A), bearings layout (B) and a pier P1 cross-section with reinforcement layout (L'Aquila) (C). For DCSS, the reported friction coefficient is that associated with the highest nominal pressure (see Section 4.3) and radius is the equivalent single-curvature one.

high-damping rubber bearings (HDRB) and DCSS, in L'Aquila (high seismicity). In Naples (medium seismicity), all three solutions are considered because they are viable in practice, but the TO is designed for high ductility with more demanding reinforcement details, rather than for low ductility as in Milan. Concrete, reinforcement and structural steel classes are C28/35, B450C and S355W, respectively. Note that for the TO configurations, only one bearing is fixed in the transverse

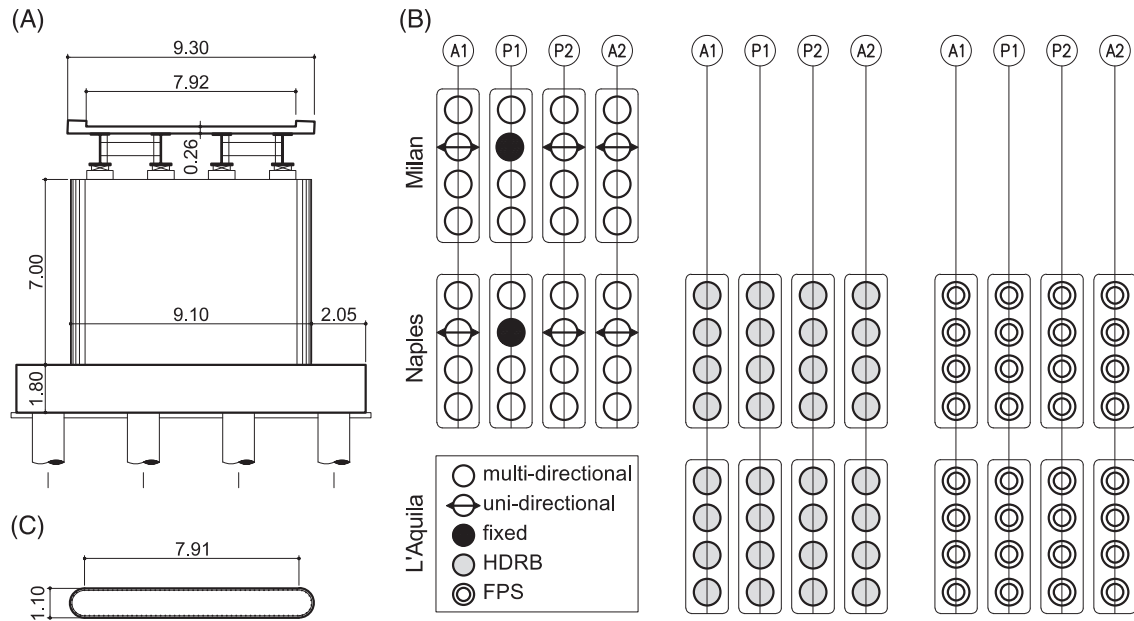


FIGURE 5 Traditional seat-type abutment overpass: deck cross-section (A), bearings layout (B) and pier cross-section (C).

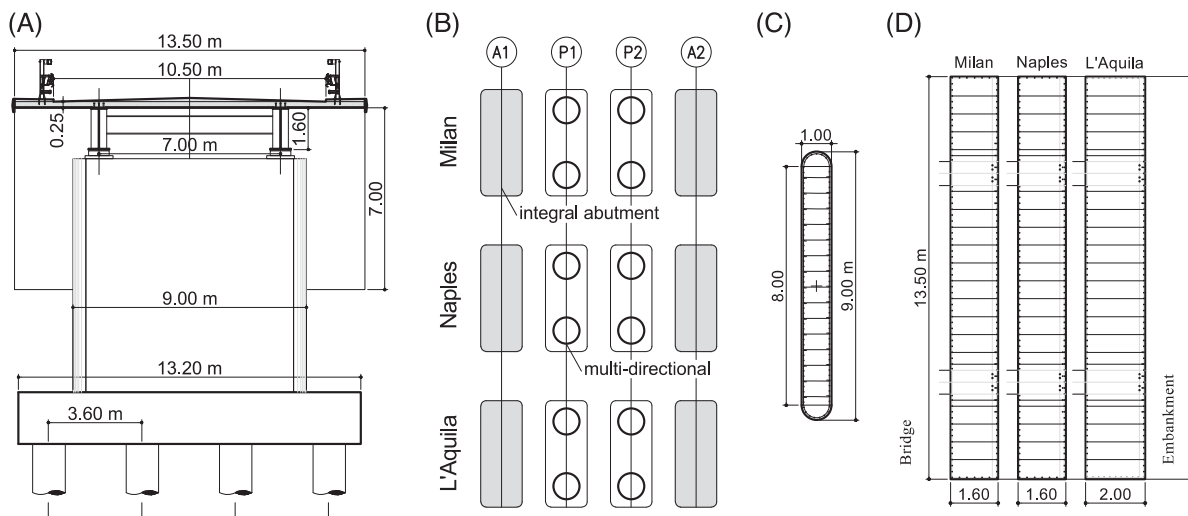


FIGURE 6 Integral abutment overpass: deck cross-section (A), bearings layout (B), pier (C) and abutment cross-section (D).

direction. Both this solution and one with more fixed bearings are adopted in practice, depending on deck width and magnitude of expected transverse deformations.^{29,30}

The integral abutment highway overpass is a straight three-span (19 + 38 + 19 m) bridge with steel-concrete deck continuous over the piers, where it is supported by multi-directional flat sliding bearings.³¹ As shown in Figure 6B, it is fully joined to the 7 m-tall RC abutments resting on a single row of four piles of diameter 1.2 m. The latter presents an RC circular cross-section with a diameter of 1.2 m. Concrete, reinforcement and structural steel classes are C32/40, B450C and S355W, respectively.

Due to the lack of specific provisions in the Italian code for integral bridges, in accordance with the latest draft of the second-generation Eurocode 8 Part 2,³² seismic design was based on a seismic analysis of a simplified numerical representation of the soil-bridge system, with reference to an iterative linear method in which the soil-abutment contact pressures are a function of the abutment displacement.³³ Note that traffic and seismic analyses were carried out after modelling the effective construction sequence, as a nonlinear staged construction in Sap 2000.

TABLE 2 Mechanical properties of the subsoil in L'Aquila, Naples and Milan.

Site	Layer –	Description –	z_b (m)	γ (kN/m ³)	K_0 –	c' (kPa)	φ' (°)	S_u (kPa)	$V_{S0,m}$ (m/s)
L'Aquila	LA1	Silt	3.0	20.0	0.56	10.0	26	75	180
	LA2	Silt	10.0	20.0	0.59	10.0	24	150	256
	LA3	Clay	18.5	20.0	0.59	10.0	24	300	295
	LA4	Stiff clay	95.0	20.0	0.59	10.0	24	300	825
	bedrock	–	–	22.0	–	–	–	–	1000
Naples	N1	Sand and debris	5.0	20.0	0.41	0.0	36	–	360
	N2	Silty sand	30.4	18.5	0.41	0.0	36	–	389
	N3	Yellow tuff	47.4	17.0	–	1750.0	0	–	704
	bedrock	Green tuff	–	22.0	–	–	–	–	790
Milan	M1	Gravelly sand	26.0	20.0	0.46	0.0	33	–	252
	M2	Clay	70.0	20.0	0.43	0.0	35	–	400
	bedrock	–	–	22.0	–	–	–	–	1000

4 | MODELLING FOR SEISMIC ASSESSMENT

The hazard-consistent input ground motions were all pre-processed via one-dimensional (1D) SRA before being employed in the MSA. 3D models for MSA were set up via OpenSees software.³⁴ Modal analysis of these models, after application of gravity loads, led to the vibration periods in Table 1, which also reports the conditioning periods used in ground motion selection.

Some remarks are due on the period values. As it regards the TVs, their stiffness in the transverse direction is the same at all sites (piers' size is governed by slenderness), resulting in the same T_Y period. In the longitudinal direction, T_X in Milan is longer because, due to lower seismicity, there is no need to add the viscous dampers (Figure 3B), whose secant stiffness is instead considered in Naples and L'Aquila. Thus T_X in L'Aquila is higher than in Naples because the dampers have the same force threshold, but displacements are larger. For the same reason, that is, inclusion of the secant stiffness of the viscous dampers in the period determination, T_X for the SV in Milan is much shorter than in Naples and L'Aquila, where the curved slider isolators are employed. Finally, note that the IABs' periods are the first 'structural' periods, that is, those most correlated in the X and Y directions with structural response in the intensity range of interest (in the longitudinal direction, the fundamental mode is usually a 'soil deposit' mode that deforms less the structure). They depend on both structure and soil/embankment stiffness. In Milan and Naples, the structure is the same and the shorter period in Milan is due to the upper layer M1 stiffer than N1 (see Table 2). In L'Aquila the abutment wall thickness is larger, to accommodate larger design moment at the deck-abutment joint, and this results in a shorter period.

4.1 | Soil profiles and site response analysis

The subsoil profiles reflect territorial features obtained by several sets of experimental data available for the sites of L'Aquila,^{35,36} Naples^{37,38} and Milan.³⁹ For all sites, the ground water table is located at a depth of 2 m from ground level. The stratigraphy and variation of the small-strain shear wave velocity, V_s , with depth are depicted in Figure 7, together with the pile foundations of the TV and traditional overpasses (profiles for the other cases can be found in Franchin et al.²²). In the saturated region, the small-strain compression wave velocity was assumed equal to that of the pore water, $V_p = 1500$ m/s, while above the water table it was related to the shear wave velocity of the soil skeleton through the expression $V_p = V_s \times [2 \times (1-\nu)/(1-2\nu)]^{0.5}$, where ν is the Poisson ratio taken equal to 0.2. The mechanical properties of each layer are summarised in Table 2, where z_b indicates the depth of the lower boundary of the generic layer with respect to the ground level at abutment A1, γ is the soil unit weight, c' and φ' are the cohesion and the angle of shearing resistance, S_u is the undrained shear strength, and $V_{S0,m}$ is the average value of the small-strain shear wave velocity of the generic layer.

1D free-field ground response analysis was carried out to compute the seismic motion at the effective depths, corresponding to the boundary of the volume of soil interacting with the foundation (see Section 4.6), and at the foundation level of the geotechnical systems (abutment and pier foundations). To this end, a 1D subsoil model was defined at each

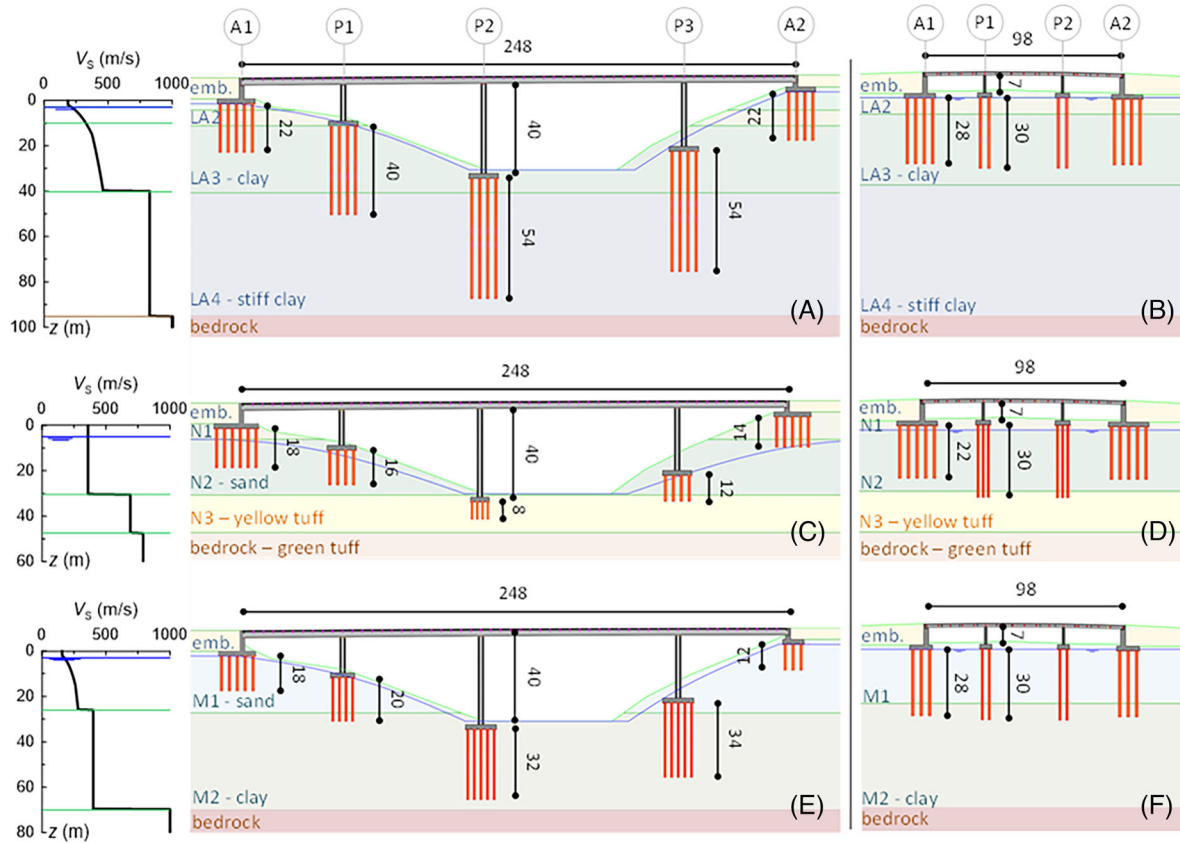


FIGURE 7 Layering and profiles of the small-strain shear wave velocity of the soil, V_s , in the case of the tall viaduct (A,C,E) and the traditional overpass (B,D,F) in L'Aquila (A,B), Naples (C,D) and Milan (E,F). Lengths in meters.

support of the soil-bridge layouts. Overall, 64,800 dynamic analyses were carried out, considering 27 soil columns subjected to the three components of the 20 records selected for each stripe and conditioning period.

The horizontal motion was assumed to be produced by shear waves whereas the vertical one by compression waves. The records were applied to the base of the soil columns accounting for the bedrock compliance.⁴⁰ The analysis was of the equivalent visco-elastic type in the frequency-domain. As per the horizontal motion, the relationships proposed by Vucetic and Dobry^{41,42} and Seed and Idriss⁴³ were used for fine- and coarse-grained soils, respectively, to simulate the dependence of the shear modulus and damping ratio on the strain amplitude. Since the soil below the foundation levels is entirely saturated, a 1%-damped linear elastic behaviour was instead assumed for the vertical motion as the propagation of compression waves is essentially controlled by the volumetric stiffness of the pore water.

The site effects concerning the horizontal motion were seen to be quite pronounced. For instance, Figure 8 compares the elastic response spectra of the motion computed at the effective depth of abutment A1 of the TV in L'Aquila with the spectra of the input motions for three representative IMLs (2, 7 and 9) and relative to a conditioning period $T_c = 1.0$ s. For the present case, the fundamental period of the soil deposit at small strains is equal to 0.54 s, while it elongates to about 0.7 and 0.8 s for the analyses carried out for IML7 and IML9, respectively, as an effect of the nonlinear behaviour of the soil. In fact, this period lengthening is reflected closely by the shift in the average predominant period of the motions obtained from the SRA.

4.2 | Deck

All the considered archetypes are made up of composite steel-concrete decks. This deck type exhibited an unsatisfactory behaviour in past earthquakes because of the activation of local failure modes of the transverse stiffeners,^{44–49,50,51} as a function of the deck-to-piers stiffness ratio.^{52–54} For this reason, an investigation was preliminarily performed on the deck

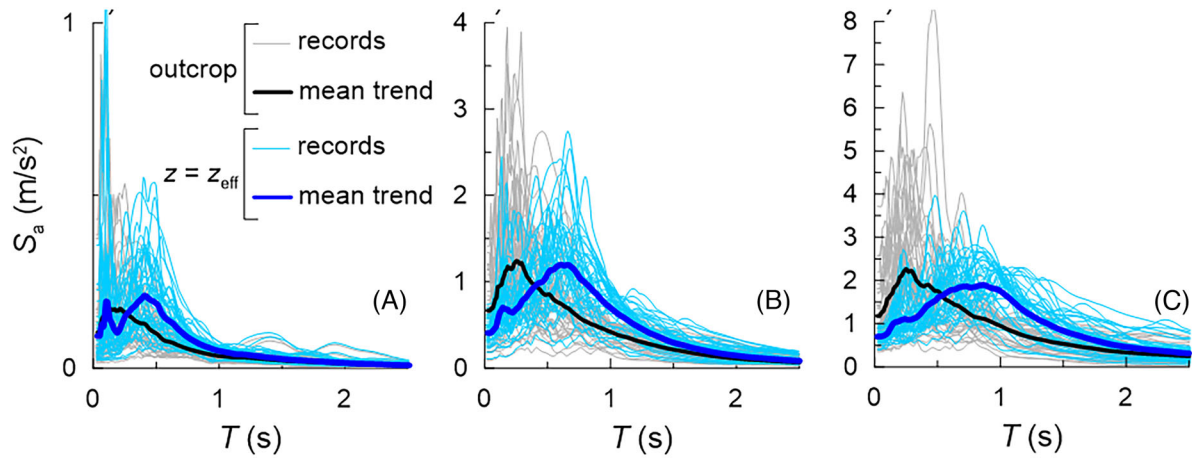


FIGURE 8 5%-damped elastic response spectra of the horizontal ground motions at the outcrop and effective depth, in correspondence of abutment A1 of the tall viaduct in L'Aquila, for IML 2, 7 and 9, in panels (A), (B) and (C), respectively. Conditioning period $T_c = 1.0$ s.

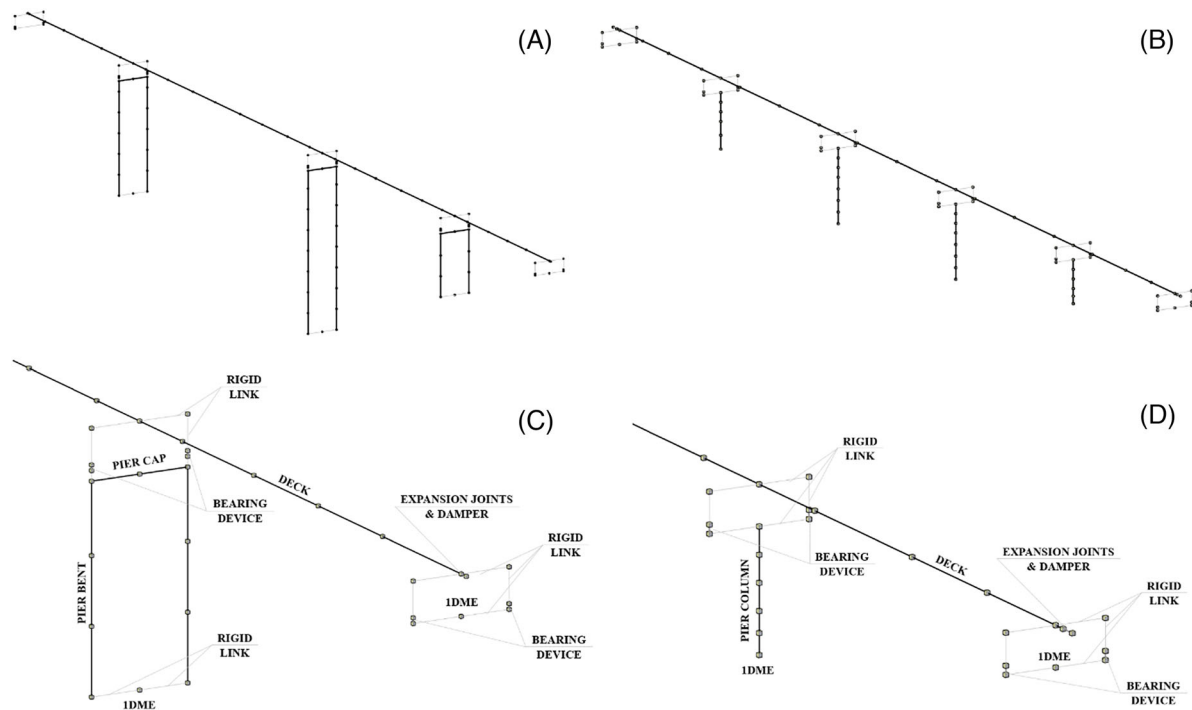


FIGURE 9 3D views of frame models for nonlinear assessment of (A) tall and (B) shallow viaduct and (C,D) relative models detail.

of the TV (the only typology having truss-type transverse stiffeners) to assess the susceptibility to such local failure.²² Non-linear static analyses were carried out on a refined finite element model of the deck, applying first the gravity loads and then simulating the seismic actions through a mass proportional distribution of horizontal forces at the slab level. The results demonstrated that the deck exhibits an almost linear behaviour up to the attainment of the shear forces causing the bearing's collapse. Consequently, a computationally efficient elastic beam-like modelling was adopted. For all seismic scenarios the elastic behaviour of the deck was checked a posteriori with reference to a plastic threshold of the slab reinforcement occurring at the smallest of two distances measured from the edge: either one-tenth of the width or the distance to the nearest junction with a steel girder web.

As a result, 3D frame models were used for all case studies. Figure 9A,B show the overall element connectivity for the models of the tall and SVs, respectively. Figure 9C,D focus on the end region of tall and SVs, respectively, to better

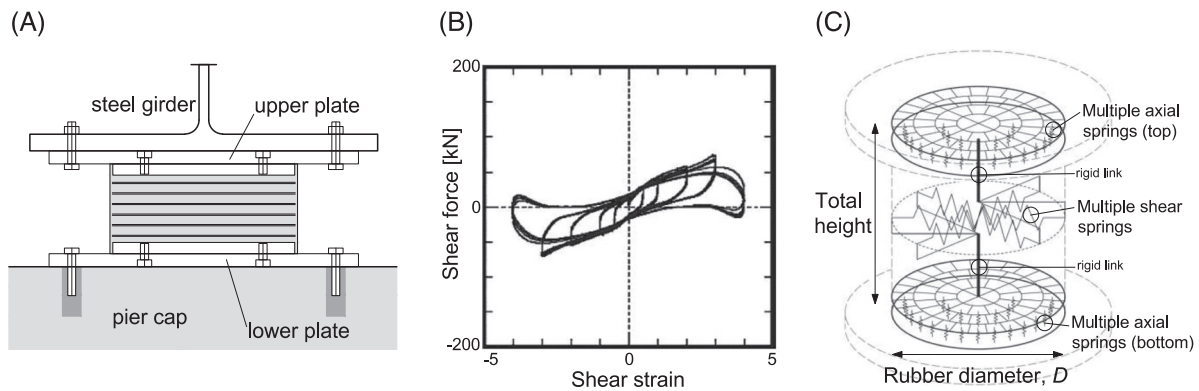


FIGURE 10 High-damping rubber bearing (A), typical force-deformation loops (B) and multi spring mechanical model (C), adapted from Ishii and Kikuchi 2019).

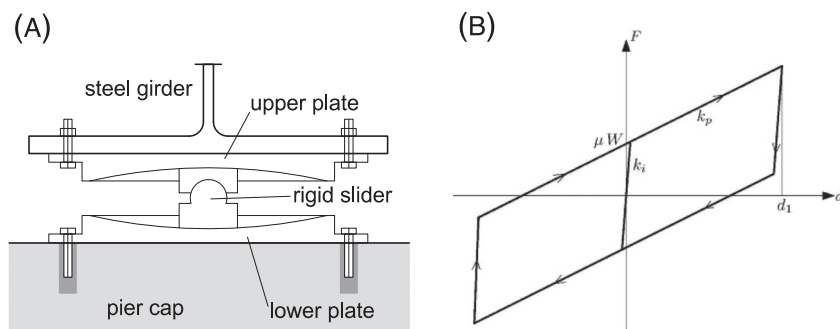


FIGURE 11 DCCSS isolator unit (A), force-displacement loop (B).

highlight the rigid link layout and the locations of anti-seismic devices (Section 4.3), bearing devices and expansion joints (Section 4.4), and macroelements (Section 4.6). The spans are discretised considering the variation of the deck cross-section along the longitudinal axis.²² The elements are placed at the average bridge deck centroid and bearing devices are offset to their actual position through *rigidLink* elements. The other components of the global bridge models are described, in an essential manner, in the following.

4.3 | Anti-seismic devices

Three typologies of anti-seismic devices were considered: HDRB and DCCSS, and axial viscous dampers employed at the abutments in some viaduct configurations.

The so-called KikuchiBearing two-node element⁵⁵ was adopted for HDRBs, as illustrated in Figure 10, to reproduce a nonlinear coupled response in the horizontal and vertical direction accounting for the reduction of horizontal stiffness with increasing vertical load and horizontal displacement. The KikuchiAikenHDR uniaxial material⁵⁶ was assigned to the shear springs in the horizontal plane, calibrated to reproduce rubber compounds typically used by Italian manufacturers.⁵⁷ The AxialSP material was instead used for the axial springs, calibrated on the vertical stiffness of the adopted devices.

The SingleFPBearing element illustrated in Figure 11 was adopted for the DCCSS isolators with the modifications described in Ponzo et al.⁵⁸ A frictional model that describes the variation of the friction coefficient μ with axial force and velocity⁵⁹ was used for simulating rocking and torsional effects on the nonlinear response of the isolator (the friction value in Figure 4 is the value at maximum allowable pressure for high velocity). Temperature, stick-slip breakaway and second-order effects were neglected. The occurrence of over-stroke events was monitored during the analysis, verifying that the effect was marginal and limited to a few cases at the highest seismic intensity only. Details, for both HDRB and DCCSS devices, are given in Franchin et al.²²

For what concerns viscous dampers, employed at the abutments of both the tall and SVs in Milan and for the shallow one in Naples, these are of the cylindrical viscous damper type, that exploit the reaction force of silicone fluid forced to

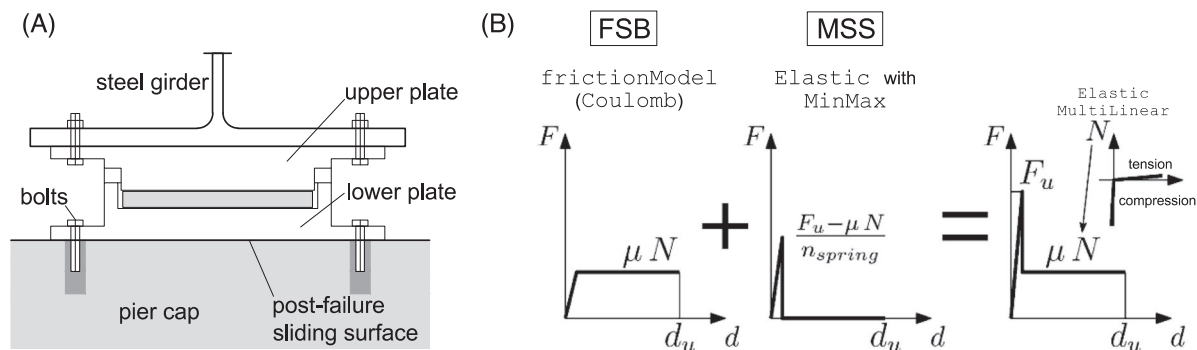


FIGURE 12 Fixed bearings: (A) bearing section, (B) mechanical model.

flow through an orifice. They have a non-linear force-velocity law, that is, $f = cv^\alpha$, with typical value $\alpha = 0.15$. They have been selected from catalogue, based on maximum force and required stroke.²²

4.4 | Conventional bearings

Three typologies of non-seismic bearings have been considered: fixed, mobile uni-directional and multi-directional bearings. To describe their inelastic response, beyond the service conditions (needed for the MSA, which is carried out also at intensities higher than the design one), numerical models for conventional bearings are developed, following Cardone.⁶⁰

As per the fixed bearings and the fixed direction of unidirectional bearings, in agreement with the experimental data,⁶¹ the horizontal response is assumed elastic up to shear failure, that occurs when the weakest between the upper-plate to steel girder and the lower-plate to pier cap connection fails (Figure 12A), followed by frictional response, with either the steel girder sliding on upper steel plate (followed by steel-to-steel friction) or the lower steel plate sliding on the pier cap (followed by steel-to-concrete friction). Considering that anchor bolt failure at the pier-cap connection emerged as the prevalent shear failure mode for these bearings, in practice a single value of 0.4 was assumed for the friction coefficient. Hence the adopted mechanical model (Figure 12C) consists of two elements in parallel: a multipleShearSpring (MSS) and a flatSliderBearing (FSB). The former describes the initial horizontal isotropic elastic behaviour, while the latter describes the axial and the post-failure horizontal behaviour. A MinMax Elastic uniaxial material was assigned to the radial springs of the MSS model, with a maximum load threshold equal to the maximum shear resistance (F_u) minus the friction force (μN). The displacement associated with the shear resistance (d_{lim}) is taken equal to 1 mm.⁶² A normal compression-only spring characterised by a very high vertical stiffness (three orders of magnitude larger than the elastic horizontal stiffness) was used for the axial direction (ElasticMultiLinear). The post-failure condition was calibrated to reproduce sliding up to the displacement limit corresponding to the device unseating (d_u). The velocity and pressure dependent friction coefficient model⁵⁹ was adopted also in this case.

As per the multidirectional bearings, their behaviour is in principle frictional with three increasing levels of friction: up to a displacement corresponding to the attainment of a contact pressure of 60 MPa, d_e , the friction coefficient, μ_e , can be taken equal to the nominal value for PTFE-stainless steel friction under service conditions (in the order of 1%); once d_e is exceeded, the friction coefficient increases to μ_1 , which can be taken equal to $1.3\mu_e$, based on experimental results⁶³; this is still a low value, corresponding to a stage where nominal displacement capacity is exceeded and contact pressure is increasing above maximum design levels, but there is still contact between the sliding surfaces; as horizontal displacement further increases, the contact surface between PTFE and stainless steel reduces until it can be deemed to be lost, for a displacement d_1 herein assumed equal to $(D + C)/2$, where D is plate width and C is the bearing pot diameter. In this last stage, reference to the steel-concrete friction coefficient μ_2 can be made, reflecting sliding of the upper plate on the concrete pier cap. The actual numerical modelling, shown in Figure 13B, is simpler since the difference between μ_e and μ_1 is negligible, and therefore disregarded, while d_1 is never exceeded at all sites and for all intensities. The single μ_1 value was therefore adopted. The velocity and pressure dependent model⁵⁹ was adopted also in this case.

Finally, the horizontal response of longitudinal unidirectional bearings derives from the combination of the modelling techniques presented above.

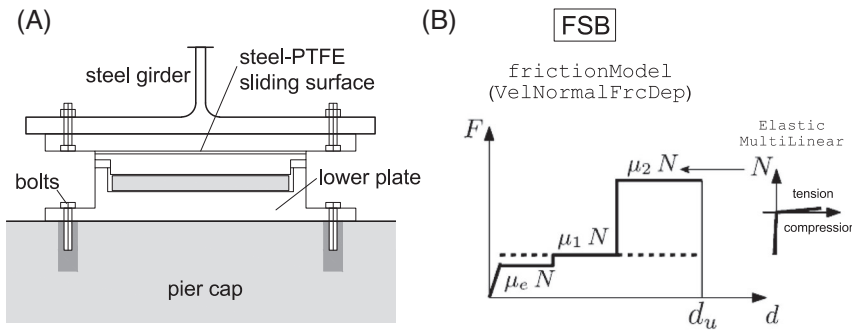


FIGURE 13 Mobile bearings: (A) bearing section, (B) mechanical model.

4.5 | Piers

Piers are modelled as fibre-section beam-column elements with displacement-based formulation accounting for both geometrical non-linearities and distributed plasticity. The behaviour of the fibres is described by the materials *Concrete01* and *Steel01* in the OpenSees library. For the TV (Figure 3A), pier caps connecting the top of both vertical column bents are modelled with elastic beam elements with secant ‘cracked’ stiffness (Figure 9A,C). For the SV (Figure 4A), rigid links connect the top node of single column bents to the bearing devices, and the tapering cross-section towards the top is described with multiple prismatic elements with increasing cross-section (Figure 9B,D).

4.6 | Soil-structure interaction

4.6.1 | Viaducts and non-integral overpasses

The frequency- and amplitude-dependent effects of dynamic SFSI are considered by introducing uniaxial, inertial macroelements (1DME) at the base of each support in the global structural models. The macroelements follow the framework proposed in Gorini et al.^{64,65}: they are perturbed by the seismic motion computed through the site response analysis, at the effective depths, z_{eff} , of the geotechnical systems taken as $10D$ ($D = \text{pile diameter}$) for the piers’ foundations,⁶⁶ and as $\max\{L_f, 10D\}$ for the abutments’ (where L_f is the longitudinal width of the abutment foundation).^{64,65}

To simulate amplitude-dependent effects, a linearly elastic-perfectly plastic constitutive law was assumed for the 1DMEs as an extremely manageable numerical tool readily adaptable to different configurations. For the abutments, the so-called 1DME-A relates the interaction force, Q_i , exchanged between the deck and the front wall to the corresponding displacement, q_i , in the i^{th} global degree of freedom of the soil-abutment system (Figure 14A). For the piers, the 1DME-P expresses a relationship between the force or moment, $Q_i = Q_1, Q_2, Q_3, Q_{R1}$ or Q_{R2} , exchanged between the pier and the foundation slab (Figure 14B), and the corresponding displacement or rotation, q_i . The frequency-dependent response exhibited by both abutments and soil-foundation systems was simulated by combining the 1DMEs with the sum of the foundation masses and the modal masses of the geotechnical systems.

For the abutments, the ultimate resistance is computed through the analytical model proposed by Gorini et al.⁶⁷ The expected loading path includes the two stages in Figure 14A: (a) the initial application of the static forces transferred by the deck and (b) the subsequent increment of the force along the considered degree of freedom of the 1DME-A. As for the masses, the longitudinal one, m_1 , is taken as that of the volume of the embankment involved in the failure mechanism under active limit conditions, according with the Mononobe-Okabe method.^{68,69} The participating masses in the transverse and vertical directions, m_2 and m_3 respectively, are taken as the masses of the abutment and of the soil fill resting on the footing. Finally, the elastic stiffness of each 1DME-A is computed as $4\pi^2 \times m_i / T_i^2$, where the small-strain vibration periods, T_i , of the soil-abutment system are obtained by means of analytical solutions.⁷⁰ The elastic response of the 1DMEs is regarded as intermediate between the small-strain and failure conditions, leading to the choice of an operational value of the elastic stiffness equal to 80% of the initial stiffness.⁷⁰ The resulting piecewise linear relationship is shown in Figure 14C.

For the piers’ foundations, the multiaxial ultimate resistance is computed by using the ultimate limit state surface model by Gorini and Callisto.⁶⁶ In terms of load path, in stage b) the horizontal forces, Q_{1-2} , increase together with the relative moment transmitted to the foundation, calculated for this purpose as $Q_{1-2} \times h_p$ ($h_p = \text{height of the pier}$). The mass of each

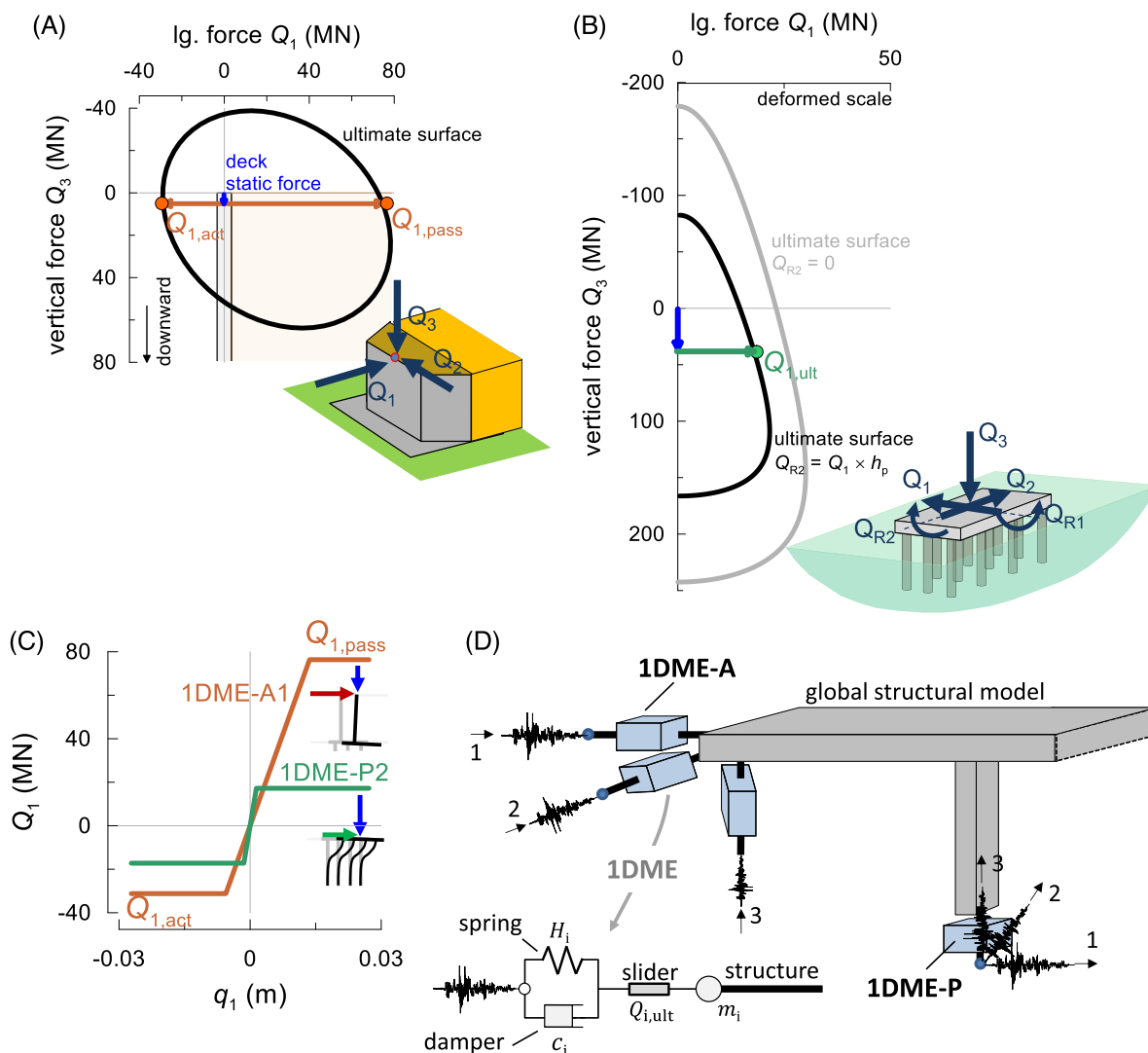


FIGURE 14 Loading paths for the evaluation of the ultimate capacities of the 1DME considering the ultimate limit state surfaces of the (A) soil-abutment and (B) soil-piles systems; (C) longitudinal force-displacement relationships of the 1DME for abutment A1 (1DME-A1) and pier P2 (1DME-P2) of the tall viaduct in L'Aquila and (D) schematic representation of the relative numerical modelling in the global structural model.

1DME-P is determined as a function of the elastic stiffness and first-mode vibration period, obtained using the commercial software DYNA.⁷¹ The resulting participating mass of the soil-piles system is summed to the mass, for the translational response, and to the rotational inertia for the rocking response to get the total mass assigned to the 1DME-P. Finally, an operational secant stiffness equal to 80% of the initial one is assigned to the 1DME-P.

In the global structural model, the 1DMEs are assigned to *twoNodeLink* finite elements available in OpenSees, according to the layout depicted in Figure 14D. Viscous dampers are connected in parallel to the 1DMEs to reproduce the hysteretic and radiation damping preceding the attainment of the ultimate resistance of the foundation. The damping coefficients are calibrated on the masses and stiffnesses of the corresponding 1DMEs, assuming a damping ratio ξ varying from 2% to 5% as the intensity of the ground motion rises (i.e., this viscous component of dissipation is IML-dependent and is calibrated as the damping in the volume of soil around the foundation, as obtained from the 1D site-response analyses, averaged overall motions at each IML).

The connection between the deck and the 1DME-A is shown in Figure 15A: it consists of a parallel arrangement of the appropriate bearing or anti-seismic device element with an elasto-plastic gap element. The latter models the contact between deck and abutment wall after failure of the bearing and closure of the gap. Its stiffness and resistance (Figure 15B) were established based on technical recommendations.⁷²

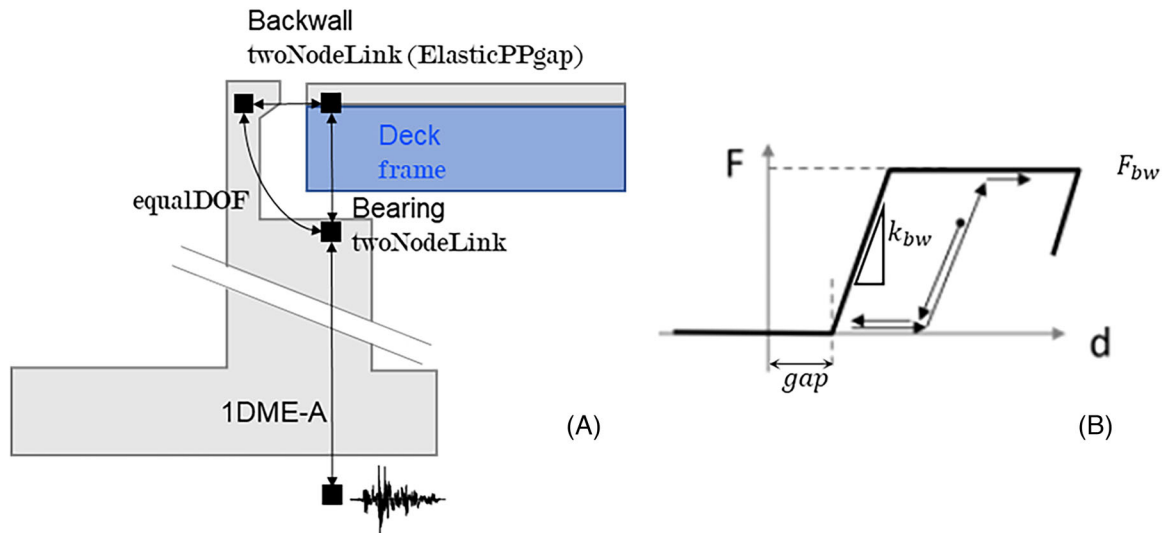


FIGURE 15 Deck-abutment connection through bearing and gap elements: (A) general arrangement, (B) backwall force-displacement law.

4.7 | Integral overpasses

In the case of integral abutment overpasses, the contact between the flexible abutment and the soil is modelled with a nonlinear Winkler approach.^{73,74} More details can be found in Franchin et al.²²

5 | PERFORMANCE LEVELS

Two performance levels, defined herein ad-hoc for the seismic reliability evaluation, are considered: Short-term *usability-preventing damage* (UPD) and long-term *usability-preventing damage* or, more briefly, *severe damage* (SD). The UPD performance level is associated with light/limited damage to structural elements or damage to non-structural components, following which traffic is either easily restored in the short term or partially guaranteed/barred only for certain categories of vehicles. The SD performance level is deemed to be attained when severe/extensive damage to structural elements occurs; damage is still repairable but closure to traffic for repair works will last for a longer time.

Exceedance of these performance levels is defined in terms of the maximum demand to capacity ratio (D/C) over a range of possible component failure/damage modes. Table 3 summarises the failure modes, engineering demand parameters (EDPs) and associated limits assumed for viaducts and traditional overpasses. For integral overpasses, different assumptions have been made for what concerns failure modes and EDPs, listed in Table 4, in accordance with their peculiar structural scheme and behaviour. In particular, the analyses confirm that some structural members remain elastic for all intensities and are not included in the D/C checks (the deck, which is stronger of the abutment wall at all sites, and the piers, which only offer vertical support through multi-directional bearings).

6 | RESPONSE

MSA was performed for all the archetype bridges for the low (IML1-IML3), medium (IML4-IML7) and high (IML8-IML10) seismic intensities introduced in Section 2. As expected, all members meet code provisions at the design seismic intensity, which coincides with IML6 ($T_R = 1000$ years, about equal to the 949 years employed in design). It is then interesting to look at the response for levels higher than the design one. To this end, and for the sake of brevity, Figure 16 shows selected response quantities of the TV for one of the twenty, three-component, ground motions from IML9 to illustrate the qualitative aspects of its dynamic response at extreme seismic motion intensities (L'Aquila site). The five columns correspond to the alignment of the five supports, from abutment A1 on the left to abutment A2 on the right. The first two rows show axial force and corresponding displacement in one of the two devices at each support, respectively. The

TABLE 3 Engineering demand parameters and associated thresholds for both performance levels: Viaducts and traditional overpass bridges. Notes: d_e = UPD limit displacement corresponding to the development of a contact pressure of 60 MPa between slider and steel plate; d_1 = SD limit displacement equal to upper plate radius plus slider radius; t_{pin} = vertical steel pin height; h_t = device height; t_r = total thickness of rubber layers.

Component	Usability-preventing damage			Severe damage		
	Description	EDP	Limit	Description	EDP	Limit
Cross beams	Flexural yielding	Bending moment	M_y	Attainment of a) flexural or b) shear strength	a) Bending moment b) Shear	a) M_u b) V_u
Fixed bearings and fixed direction of unidir.	Attainment of lateral strength	Force	F_u	a) Incipient unseating of upper plate from support, b) Exceedance of compression limit, c) Uplift.	a) Long. displ. b) Upward displ., c) Axial load	a) d_1 b) t_{pin} c) N_u
Multidirectional bearings	Maximum stroke exceedance	Displ.	d_e	a) Incipient unseating of upper plate from support, b) Exceedance of compression limit, c) Uplift.	a) Horiz. displ. b) Upward displ., c) Axial load	a) d_1 b) t_{pin} c) N_u
FPS (DCSS)	-	-	-	a) Incipient falling of slider from backing plate, b) Uplift, c) Exceedance of compression limit.	a) Horiz. displ. b) Upward displ., c) Axial load	a) d_1 b) $0.1h_t$ c) N_u
HDRB	-	-	-	a) Shear failure, b) Tension cavitation, c) Buckling	a) Shear strain γ_t b) Tension strain ϵ_t c) Downward displ.	a) 350% b) 50% c) $t_r/2$
Piers (Brittle mode)	Attainment of maximum strength	Shear force	V_u	Crack opening and significant residual displacements	Shear force	$0.8V_u$ post peak
Piers (Ductile mode)	Yielding	Chord rotation	θ_y	Significant residual displacements	Plasting hinge rotation	$\theta_{max} = f(\theta_u)$
Abutment backwall	Abutment-deck joint closure	Relative deck-backwall displacement	Gap	Attainment of lateral strength of abutment backwall-backfill system	Relative deck-backwall displacement	Gap + F_{bu}/k_{bu}
Foundations	a) Pile yielding, b) Residual active thrust	Top pile displ.	a) $\delta_{y,long}$ $\delta_{y,trans}$ b) $\delta_{y,es}$	Attainment of piles' ultimate rotation	Top pile displ.	$\delta_{u,long}$ $\delta_{u,trans}$

TABLE 4 Engineering demand parameters and associated thresholds for both performance levels: Integral abutment overpass bridges.

Component	Usability-preventing damage			Severe damage		
	Description	EDP	Limit	Description	EDP	Limit
Bearings (over the piers)	–	–	–	Incipient unseating of upper plate from support	Relative displacement	d_1
Abutment	Yielding @ deck-abutment joint	Curvature	ϕ_y	Intermediate between yield and ultimate @ deck-abutment joint	Curvature	$\phi_{max} = f(\phi_u)$
Foundations	Yielding @ piles' head	Curvature	ϕ_y	Intermediate between yield and ultimate @ piles' head	Curvature	$\phi_{max} = f(\phi_u)$

response of the two devices or bearings, whose model is axial-load-dependent, as explained in §4.3, differs due to the axial force variations associated with deck torsion (the vertical component of ground motions affects equally the two devices). The third row shows the longitudinal shear force in the same devices, negligible and associated with the steel-Teflon friction at the abutments and on pier P1, larger over piers P2 and P3 where the fixed bearings are used. Panel 15 shows also the total dampers' axial force at abutment A2 (both panels 15 and 25 show a maximum force of about 5000 kN, compare with Figure 3). All bearings are fixed in the transverse direction, as shown in the fourth row. Panels 21 to 25 show the force-deformation loops for all the devices, with longitudinal response in blue (cyan for the damper) and transversal response in red. Panels 26 to 28 show the moment-curvature loops at the base of the piers, while the last two rows show the axial force time-series and the shear force-deformation loops in the foundations, respectively.

As it can be seen from panels 1, 2 and 5, as well as 6, 7 and 10, due to the combined effect of larger transverse shears, and thus torsion in the deck, and larger axial stiffness of the abutment and short pier, axial force becomes zero and uplifting occurs. Also, larger transverse shear forces break the bearings at all supports except for that over pier P2 (panels 16 to 20). It is worth noting that the failure of fixed bearings was expected considering that they were designed without following the capacity design approach, in accordance with the Italian code. The piers, on the other hand, behave still substantially in the linear range (panels 26 to 28). Piers' foundation behaviour is also linear, while the abutments fail and, due to their non-symmetric response, accumulate significant inward longitudinal displacements, shown in blue in panels 34 and 38. These inward displacements are caused by the earth pressures behind the abutment and the activation of a global failure mechanism. The taller left abutment A1 also accumulates some transverse displacement, as shown in red in panel 34. These responses correspond to D/C ratios larger than one in more than one of the criteria set forth in Section 5.

Figure 17 shows the response to a selected ground motion (from IML10 seismic intensity) of the highway overpass located in Naples, with HDRB isolators. The four columns correspond to the alignment of the five supports, from abutment A1 on the left to abutment A2 on the right. Rows from top to bottom show: axial forces (panels 1 to 4) and axial displacements (5–8) in one bearing, longitudinal shear forces (9–12), transversal shear force (13–16) and shear force-deformation loops (17–20) in one bearing, moment-curvature loops in the pier base section (21–22), axial forces (23–26) and horizontal force-lateral displacement cycles (27–30) in the foundation.

Maximum displacements greater than the design displacement capacity of the device (200 mm) are recorded along the two horizontal directions. Nonetheless, RC piers remain elastic as expected for isolated bridges. Smaller heights and masses also lead to a substantially elastic response of the abutments, contrarily to what is observed for the TV.

More details on the response of all four archetype bridges and the complete set of D/C ratios as a function of the intensity at all sites can be found in Franchin et al.²² These values are used to assess reliability as explained in the following section.

7 | RELIABILITY

The failure rate, λ_f , with respect to each of the two considered performances, was calculated as:

$$\lambda_f = \int_{IM} P[f | IM = im] \cdot |d\lambda_{im}| \quad (1)$$

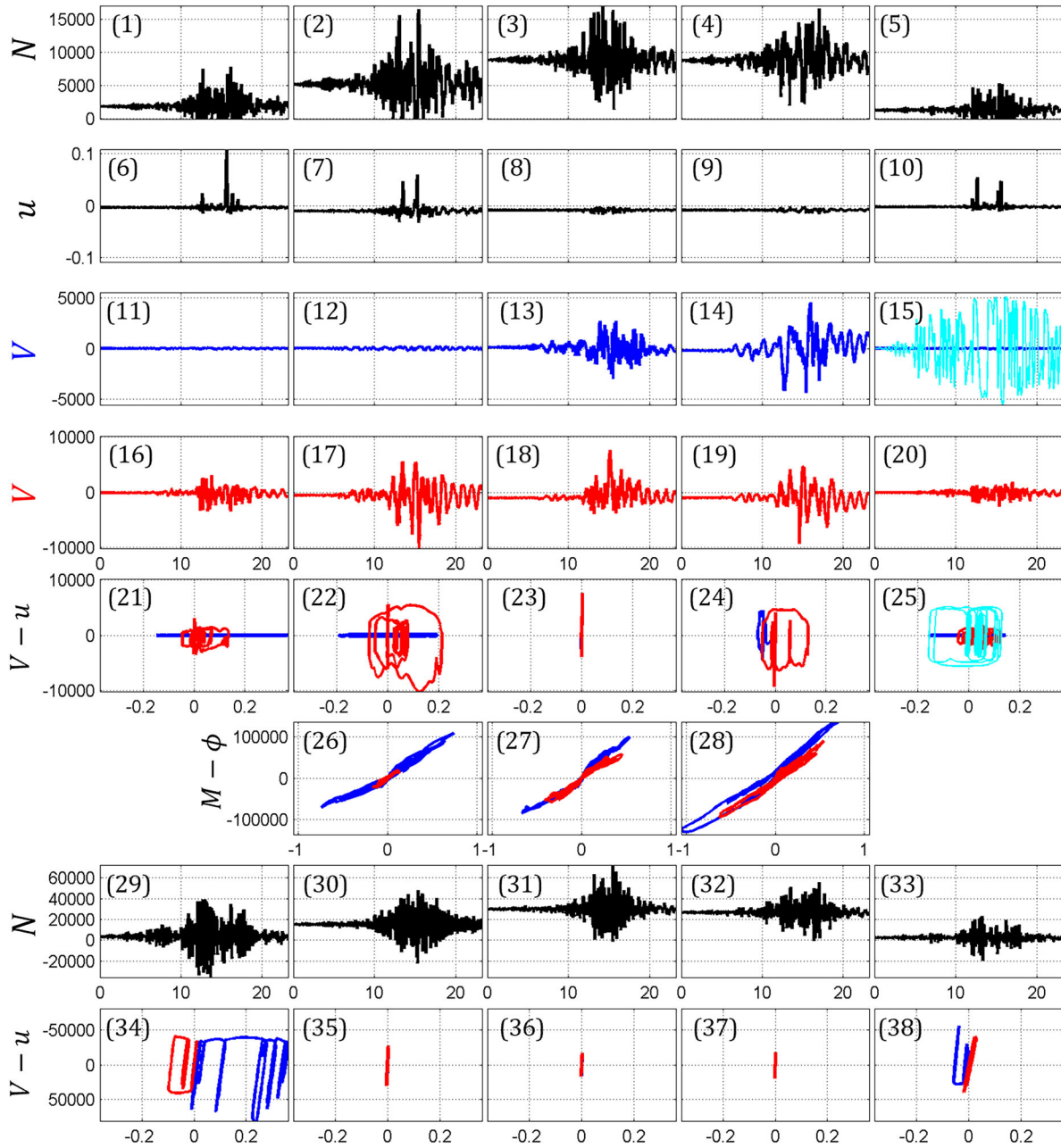


FIGURE 16 Sample response histories and force-deformation cycles for the tall viaduct subjected to one tri-component recorded motion from IML9. Black, blu/cyan and red colours denote the vertical, longitudinal and transverse direction, respectively. Cyan is associated with viscous dampers at the right abutment A2.

where $P[f|IM = im]$ is the fragility of the structural model, that is the probability of failure (i.e., onset of UPD or SD, identified as the maximum value of D/C overall considered failure modes being larger than one), conditional to $IM = im$ and $|d\lambda_{im}|$ is the absolute value of the derivative of the site-specific hazard curve times $d(im)$.

While evaluation of (1) does not require an analytical expression for the fragility, for portability of the presented vulnerability results, fragility curves were also fitted through the data from nonlinear dynamic analysis. The fragility fitting framework is that referred to as *EDP*-based according to the terminology of Vamvatsikos and Cornell,⁷⁵ where the EDP is the maximum D/C ratio. Three fragility fitting procedures were used, the same used for buildings in Iervolino et al.⁷⁶ Figure 18 reports the best fit for both limit states for all the archetypes and sites, while fragility parameters are given in Table 5. Note that some curves can be poorly constrained by the nonlinear dynamic analysis results, at the sites where a few or no failures are observed for the investigated range of intensity measures.⁷⁷ As discussed in the given reference,

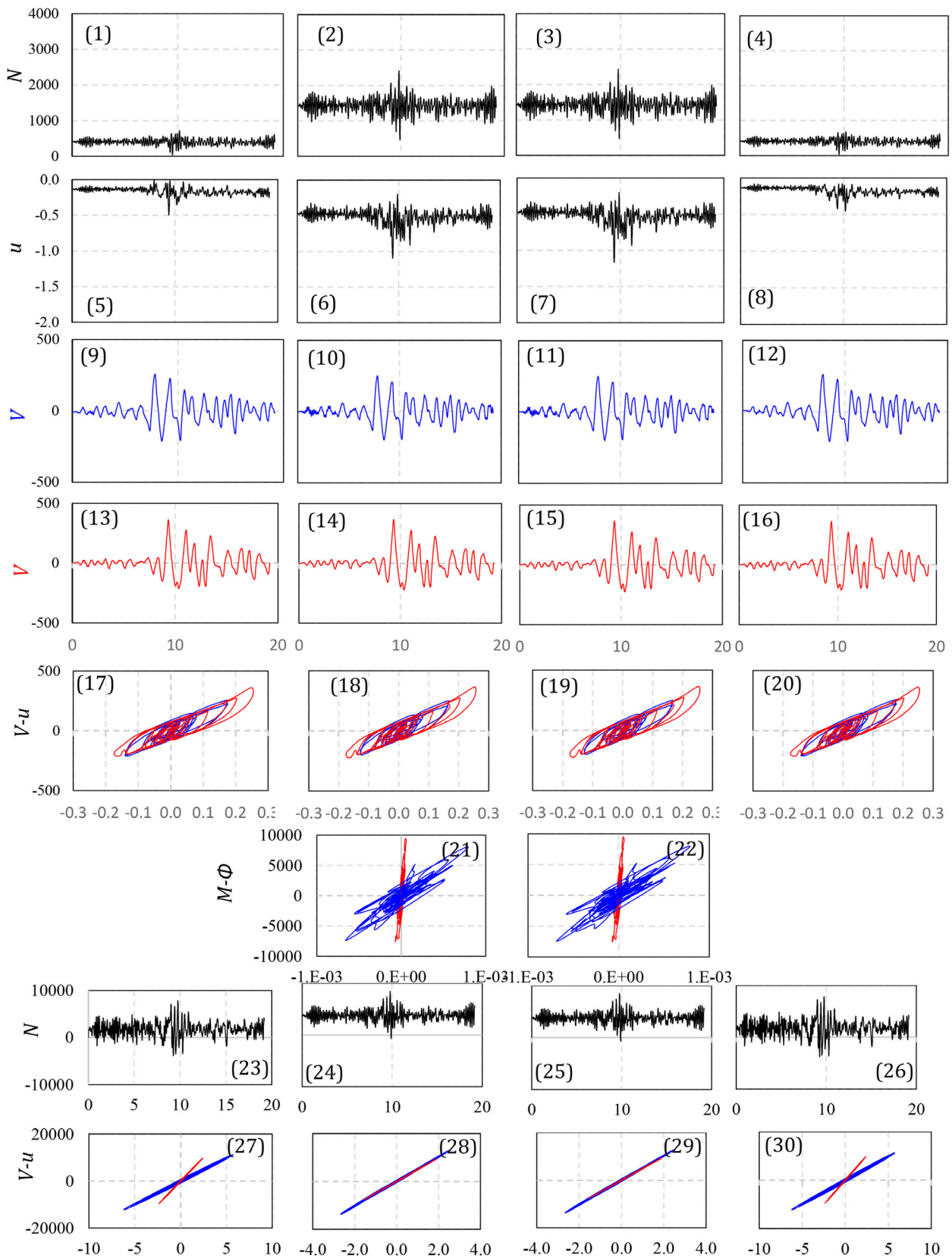


FIGURE 17 Sample response histories and force-deformation cycles for the HDRB overpass bridge located in Naples subjected to one tri-component recorded motion from IML10. Black, blu/cyan and red colours denote the vertical, longitudinal and transverse direction, respectively.

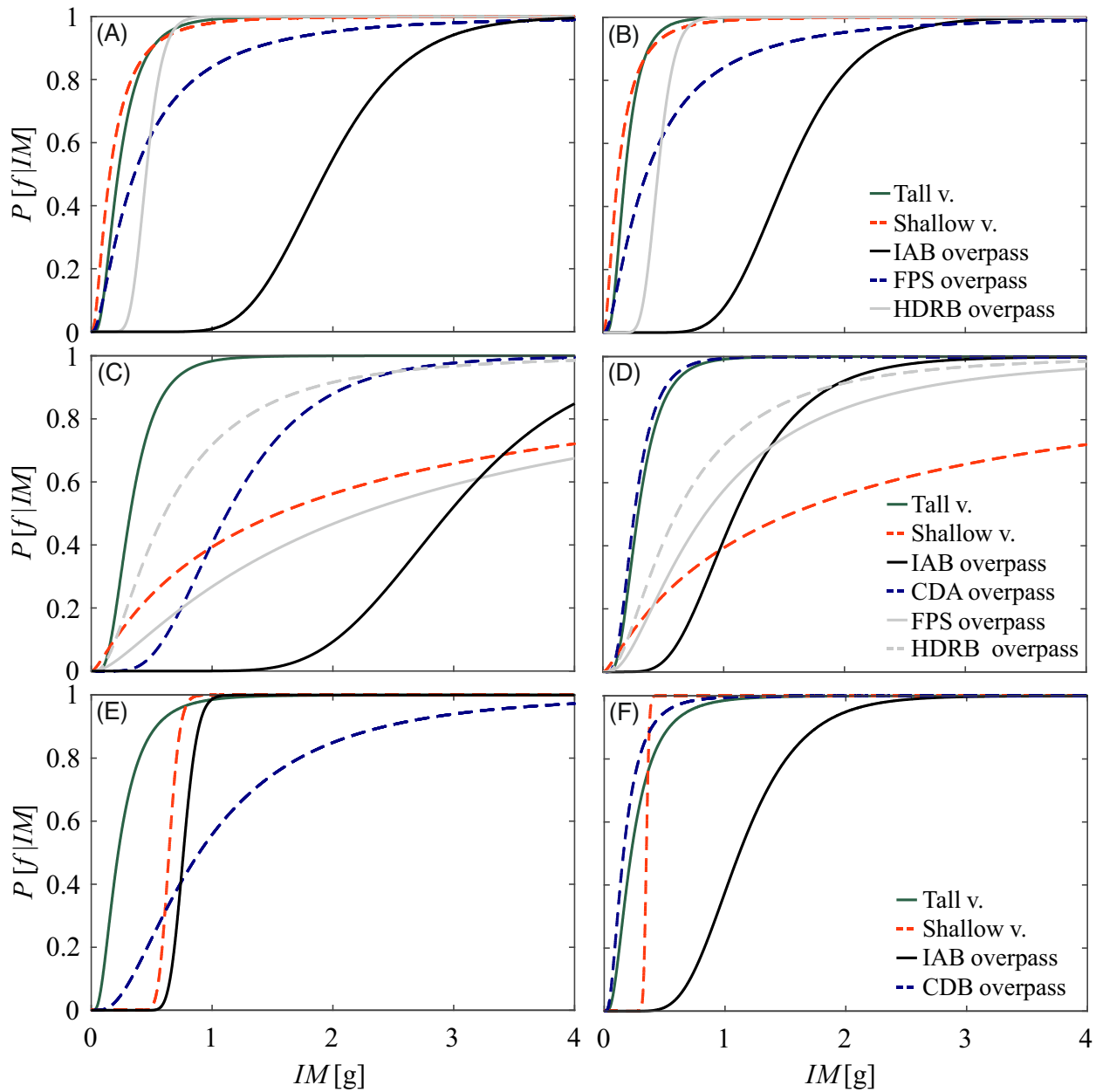


FIGURE 18 Fragility curves for the analysed bridges. Limit states: SD (A-C-E) and UPD (B-D-F). Sites: L'Aquila, Naples and Milan from top to bottom.

comparatively large uncertainty is associated with cases where no or a few failure cases ($D/C > 1$) occur. This may happen due to the intrinsic fragility of the structural model analysed or the hazard of the site. This is the case for the SD limit state for all structures in Milan (TV, SV, CDB overpass) and the integral abutment bridges in Milan and Naples. The corresponding curves are shown only for completeness (note the switch of median of fragility, with the IAB and the SV in Milan being more vulnerable than those in Naples, even considering the different soil profiles).

The results of the 15 considered cases are summarised in Figures 19 and 20. The former presents the failure rates as a function of site and therefore seismicity, while the latter shows them as a function of typology. Figure 19, in a way that is more pronounced for the SD limit state, confirms the well-known result that designing to the current code, which is based on uniform hazard, does not lead to uniform risk. Risk decreases with seismicity. In Milan, the low-seismicity site, the annual failure rate is for almost all typologies close to and mostly smaller than 10^{-5} . Overall, the annual failure rates for the considered limit states are not negligible at the highest seismicity site of L'Aquila.

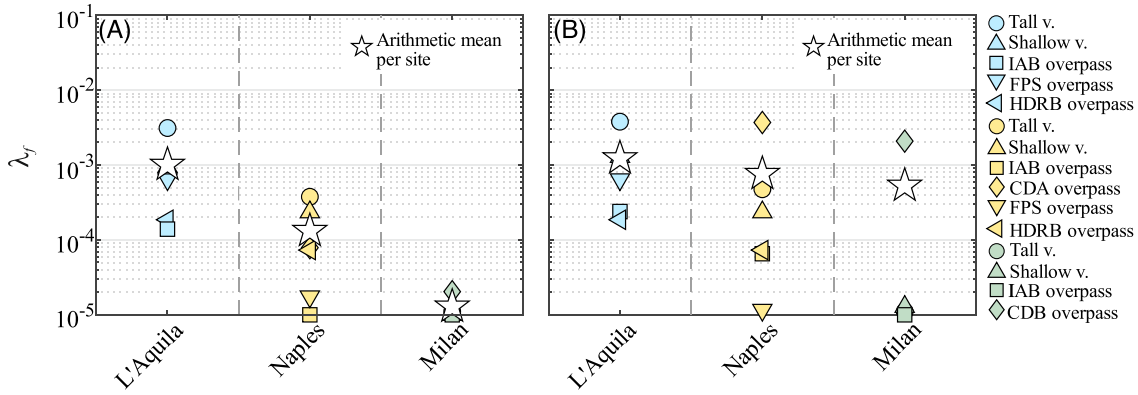


FIGURE 19 Failure rates for SD (A) and UPD (B) as a function of the design site, star is the arithmetic average of all results.

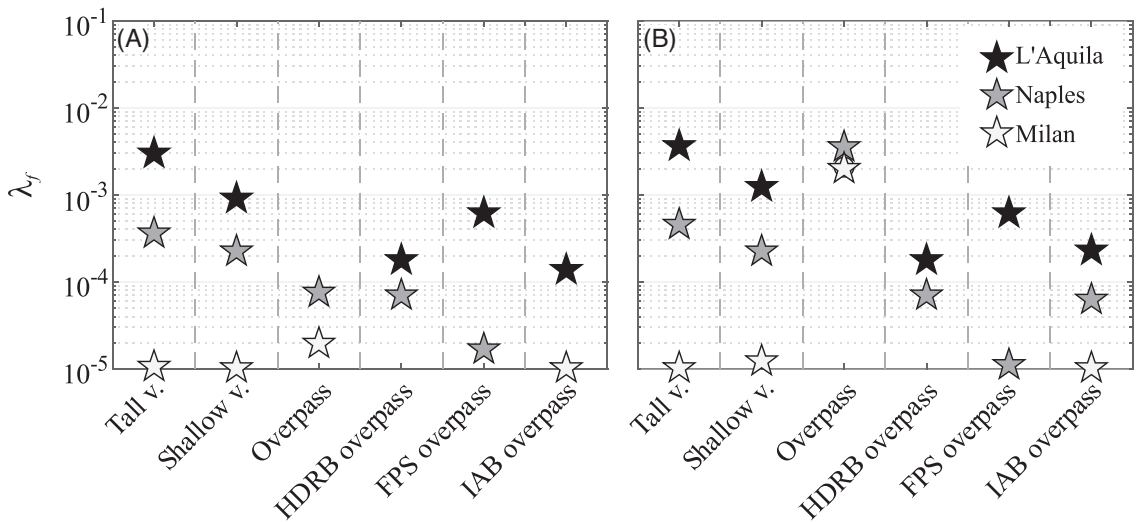


FIGURE 20 Failure rates for SD (A) and UPD (B) as a function of the structural typology.

A term of comparison is necessary to assess the failure rates. The latest draft of second-generation Eurocode 8²⁸ establishes annual maximum probability² targets for the near collapse (NC) and the significant damage (SD) limit states equal to 2×10^{-4} and $\approx 10 \times 10^{-4}$, respectively, for ordinary structures and to 1×10^{-4} and 5×10^{-4} , respectively, for bridges under or over main roads, such as the highway structures considered herein. The NC represents a condition that is more severe than that considered herein and not attained for any IML by any of the considered archetypes. The code-defined significant damage LS is the closest to the SD performance level defined herein. Figures 19A and 20A show how most failure rates, except for the TV and SV in L'Aquila, are below 5×10^{-4} .

Figure 19 also highlights a relatively large difference in reliability between typologies. Figure 20 allows appreciating better this aspect. It confirms that, within each typology, reliability decreases with increasing seismicity. It also shows, however, that traditionally designed non-isolated structures are those characterised by the larger failure rates. In L'Aquila the TV has a large value of $\lambda_f = 3 \times 10^{-3}$. The results in Figure 16, representative of results for this structure, show that the issue might be not with the superstructure design but, rather, with the design of the abutments. In fact, even though the fixed non-seismic bearings fail at the largest intensities, this does not lead to loss of support and repair is possible (continuous decks are much more resilient in this respect). For this case, what makes the bridge out-of-service are the large cumulative permanent displacements at the abutments. Of course, this is more likely in major bridges like the TV, where abutments can be themselves tall and massive. Notably, the least vulnerable structural type is the integral abutment overpass.

² For the considered values, annual probability of failure and mean annual rate of failure are numerically equivalent and treated as interchangeably herein.

8 | CONCLUSIONS

This paper presented probabilistic seismic reliability assessment of four archetype bridge structures, two viaducts and two overpasses, representative of current construction practice in Italy. These structures were placed and designed to the latest code at three sites, that is, Milan, Naples and L'Aquila, characterised by seismic hazard ranging from low-to-high in the country. Seismic reliability was then assessed in terms of failure rate for two purposely defined performance levels, employing hazard curves from site-specific PSHA and fragility obtained through non-linear dynamic analysis of response within an MSA scheme. All relevant failure modes were included, and response models describing response beyond the design level intensity were adopted. SRA was used at each support for all sites, and SFISI was modelled through inelastic inertial macroelements. The following remarks can be made based on the findings:

- MSA results confirm that all bridges designed to the code satisfy code-requirements at the design level intensity ($T_R = 949$ years, IML6 in this paper) and often beyond that.
- At the highest intensities, however, multiple failure modes occur, such as rupture of non-seismic bearing devices or accumulation of permanent displacements at the abutments.
- Seismic reliability tends to decrease as the site seismic hazard increases. This is consistent with the findings of previous studies, developed following the same framework and related to both current-code-conforming and pre-code/low-code buildings. The rate of failure at SD in L'Aquila, average overall bridges, is one order of magnitude larger than the corresponding value in Naples, which in turn is one or more orders of magnitude larger than that in Milan, where failure rates at SD are for most structures lower than 10^{-5} per year.
- The comparison of failure rates highlights also significant differences between typologies, with rates that differ, at the same site, by more than one order of magnitude. The highest failure rates are associated with the TV, which employs traditional bearings, whose rupture is expected given that they are not capacity-designed. Notably, integral abutment overpasses have rates smaller than even seismically isolated ones.
- Finally, it is noted that failure rates are generally lower, except for the tall and SV in L'Aquila, than threshold values under discussion at the European level.

ACKNOWLEDGEMENTS

This study was carried out within the activities of the ReLUIS-DPC and DPC 2019–2021 research programs, funded by the Presidenza del Consiglio dei Ministri—Dipartimento della Protezione Civile (DPC). The opinions and conclusions presented by the authors do not necessarily reflect those of the funding agency.

DATA AVAILABILITY STATEMENT

The data that support the findings of this study are available from the corresponding author upon reasonable request.

ORCID

Paolo Franchin  <https://orcid.org/0000-0002-1995-0415>

Georgios Baltzopoulos  <https://orcid.org/0000-0002-0460-6558>

Luigi Callisto  <https://orcid.org/0000-0001-9795-7420>

Luca Capacci  <https://orcid.org/0000-0002-1450-1987>

Donatello Cardone  <https://orcid.org/0000-0002-2814-7456>

Andrea Dall'Asta  <https://orcid.org/0000-0001-7482-9434>

Davide Noè Gorini  <https://orcid.org/0000-0001-6673-0071>

Andrea Marchi  <https://orcid.org/0000-0001-6645-3633>

Iunio Iervolino  <https://orcid.org/0000-0002-4076-2718>

REFERENCES

1. Calvi GM, Pinto PE, Franchin P. Seismic design practice in Italy. In: Chen W-F, Duan L, eds. *Bridge Engineering Handbook*. 2nd ed. CRC; 2014:633-660.
2. C.S.LL.PP. Aggiornamento Delle “Norme Tecniche per Le Costruzioni”. *Gazzetta Ufficiale Della Repubblica Italiana*. 2018;42. (In Italian).
3. Cornell AC. Engineering seismic risk analysis. *Bull Seismol Soc Am*. 1968;58(5):1583-1606.
4. Jalayer F, Cornell CA. Alternative non-linear demand estimation methods for probability-based seismic assessments. *Earthq Eng Struct Dyn*. 2009;38(8):951-972. doi:10.1002/eqe.876

5. Schnabel PB, Lysmer J, Seed HB. *SHAKE - A Computer Program for Earthquake Analysis of Horizontally Layered Sites*. Earthquake Engineering Research Center, University of California, Berkeley; 1972.
6. Kramer SL. *Geotechnical Earthquake Engineering*. Prentice Hall; 1995.
7. Haselton CB, Liel AB, Deierlein GG, Dean BS, Chou JH. Seismic collapse safety of reinforced concrete buildings. I: assessment of ductile moment frames. *J Struct Eng*. 2011;137(4):481-491.
8. Liel AB, Haselton CB, Deierlein GG. Seismic collapse safety of reinforced concrete buildings. II: comparative assessment of nonductile and ductile moment frames. *J Struct Eng*. 2011;137(4):492-502.
9. Iervolino I, Spillatura A, Bazzurro P. Seismic reliability of code-conforming Italian buildings. *J Earthq Eng*. 2018;22(Suppl 2):5-27.
10. Iervolino I. Foreword to the special issue for the 2019–2021 RINTC (The implicit seismic risk of existing structures) project. *J Earthq Eng*. 2022. doi:10.1080/13632469.2022.2101233
11. Ricci P, Manfredi V, Noto F, et al. Modeling and seismic response analysis of Italian code-conforming reinforced concrete buildings. *J Earthq Eng*. 2018;22(Suppl 2):105-139.
12. De Risi MT, Di Domenico M, Manfredi V, et al. Modelling and seismic response analysis of Italian pre-code and low-code Reinforced Concrete Buildings. Part I: bare frames. *J Earthq Eng*. 2023;27:6, 1482-1513. doi:10.1080/13632469.2022.2074919
13. Di Domenico M, De Risi MT, Manfredi V, et al. Modelling and seismic response analysis of Italian pre-code and low-code Reinforced Concrete Buildings. Part II: infilled frames. *J Earthq Eng*. 2023;27:6, 1534-1564. doi:10.1080/13632469.2022.2086189
14. Basoz N, Kiremidjian AS. Risk assessment of bridges and highway systems from the Northridge earthquake. Second National Seismic Conference on Bridges and Highways California Department of Transportation; and Federal Highway Administration. 1997.
15. Nielson BG, DesRoches R. Analytical seismic fragility curves for typical bridges in the central and southeastern United States. *Earthq Spectra*. 2007;23:615-633.
16. Moschonas IF, Kappos AJ, Panetsos P, Papadopoulos V, Makarios T, Thanopoulos P. Seismic fragility curves for Greek bridges: methodology and case studies. *Bull Earthq Eng*. 2009;7:439-468.
17. Avşar Ö, Yakut A, Caner A. Analytical fragility curves for ordinary highway bridges in Turkey. *Earthq Spectra*. 2011;27:971-996.
18. Borzi B, Ceresa P, Franchin P, Noto F, Calvi GM, Pinto PE. Seismic vulnerability of the Italian roadway bridge stock. *Earthq Spectra*. 2015;31(4):2137-2161.
19. Spillatura A, Kohrangi M, Bazzurro P, Vamvatsikos D. Conditional spectrum record selection faithful to causative earthquake parameter distributions. *Earthq Eng Struct Dyn*. 2021;50:2653-2671. doi:10.1002/eqe.3465
20. Lin T, Haselton CB, Baker JW. Conditional spectrum-based ground motion selection. Part I: hazard consistency for risk-based assessments. *Earthq Eng Struct Dyn*. 2013;42(12):1847-1865. doi:10.1002/eqe.2301
21. Iervolino I, Chioccarelli E, Convertito V. Engineering design earthquakes from multimodal hazard disaggregation. *Soil Dyn Earthq Eng*. 2011;31(9):1212-1231. doi:10.1016/j.soildyn.2011.05.001
22. Franchin P, Baltzopoulos G, Biondini F, et al. Seismic reliability of representative Italian code-conforming highway bridges. Final report of DPC-Reluis 2019–2021 RINTC (The Implicit Seismic Risk of Code-Conforming Structures) Project, Task Bridges. 2023. doi:10.13140/rg.2.2.25622.32329
23. Ambraseys NN, Simpson KA, Bommer JJ. Prediction of horizontal response spectra in Europe. *Earthq Eng Struct Dyn*. 1996;25(4):371-400. doi:10.1002/(SICI)1096-9845(199604)25:4<371::AID-EQE550>3.0.CO;2-A
24. Akkar S, Bommer JJ. Empirical equations for the prediction of PGA, PGV, and spectral accelerations in Europe, the Mediterranean region, and the Middle East. *Seismol Res Lett*. 2010;81(2):195-206. doi:10.1785/gssrl.81.2.195
25. SAP2000. Accessed January 9, 2023. <https://www.csiamerica.com/products/sap2000>
26. FIP. *Elastomeric Isolators (SI series) Manufacturing Catalogue*. FIP INDUSTRIALE SpA, 2008.
27. FIP. *Friction Pendulum (D series) Manufacturing Catalogue*. FIP INDUSTRIALE SpA, 2008.
28. CEN/TC250. *Eurocode 8 - Design of structures for earthquake resistance - Part 1- 1: General rules and seismic action (prEN1998-1-1_2021_ENQ,N1141)*. European Committee of Standardization. Technical Committee 250 (Sub-Committee 8); 2022.
29. Marioni A. *Bearing Devices for Bridges and Other Structures*. ITEC; 1983. (In Italian).
30. Petrangeli MP. *Design and Construction of Bridges*. 6th ed. CEA; 1996. (In Italian).
31. Torricelli F, Marchiondelli A, Pefano R, Stucchi R. Integral bridge design solutions for Italian highway overpasses. Proceedings of the Sixth International IABMAS Conference. Stresa, Italy; 2012.
32. CEN/TC250. *Eurocode 8: Design of Structures for Earthquake Resistance - Part 2: Bridges (prEN1998-2_2022_ENQ,N1182)*. European Committee of Standardization. Technical Committee 250 (Sub-Committee 8); 2022.
33. Marchi A, Franchin P. A pushover method for seismic design of Integral Abutment Bridges. Proc. fib PhD symposium, Rome; 2022.
34. Mazzoni S, McKenna F, Scott MH, Fenves GL. *OpenSees: Open System for Earthquake Engineering Simulation*. Pacific Earthquake Engineering Research Center, University of California; 2009.
35. Monaco P, Totani G, Amoroso S, Totani F, Marchetti D. Site characterization by seismic dilatometer (SDMT) in the city of L'Aquila. *Rivista Italiana di Geotecnica*. 2013;XLVII(3):8-22.
36. Santucci de Magistris F, d'Onofrio A, Evangelista L, et al. Geotechnical characterization of the Aterno Valley for site response analysis. *Rivista Italiana di Geotecnica, Anno*. 2013;XLVII(3):23-43. Patron Editore, Bologna.
37. Amorosi A, Aversa S, Boldini D, Laera A, Nicotera MV. Application of a new constitutive model to the analysis of plate load tests in a pyroclastic rock. *Int J Rock Mech Min Sci*. 2015;78(1):271-282.

38. de Silva F. *Dynamic Soil-Foundation-Structure Interaction for Masonry Towers: The Case Study of Carmine Bell Tower in Napoli. Tesi di Dottorato in Rischio Sismico*. Università di Napoli Federico II; 2016.
39. Fargnoli V, Gagnano CG, Boldini D, Amorosi A. 3D numerical modelling of soil-structure interaction during EPB tunnelling. *Geotechnique*. 2015;65(1):23-37. doi:10.1680/geot.14.P.091
40. Roesset JM. Soil amplification of earthquakes. In: Desai C S, Christian J T, eds. *Numerical Methods in Geotechnical Engineering*. McGraw-Hill, New York; 1977:639-682.
41. Vucetic M, Dobry R. Effect of soil plasticity on cyclic response. *J Geotech Engrg (ASCE)*. 1991;117(1):89-107.
42. Tubaldi E, Barbato M, Dall'Asta A. Influence of model parameter uncertainty on transverse response and vulnerability of steel-concrete composite bridges with dual load path. *ASCE J Struct Eng*. 2012;138(3):363-374.
43. Seed HB, Idriss IM. Analyses of ground motions at Union Bay, Seattle, during the earthquakes and distant nuclear blasts. *Bull Seism Soc Am*. 1970;60:125-136.
44. Astaneh-Asl A, Bolt B, McMullin KM, Donikian RR, Modjtahedi D, Cho SW. *Seismic Performance of Steel Bridges during the 1994 Northridge Earthquake*. Dept. of Civil Engineering, Univ. of California; 1994. Report No. UCB/CE-Steel-94/01.
45. Itani AM, Bruneau M, Carden LP, Buckle IG. Seismic behavior of steel girder bridge superstructures. *J Bridge Eng*. 2004;9(3):243-249.
46. Zahrai SM, Bruneau M. Impact of diaphragms on seismic response of straight slab-on-girder steel bridges. *J Struct Eng*. 1998;124(8):938-947.
47. Zahrai SM, Bruneau M. Ductile end-diaphragms for seismic retrofit of slab-on-girder steel bridges. *J Struct Eng*. 1999a;125(1):71-80.
48. Zahrai SM, Bruneau M. Cyclic testing of ductile end diaphragms for slab-on-girder steel bridges. *J Struct Eng*. 1999b;125(9):987-996.
49. Bruneau M, Wilson JW, Tremblay R. Performance of steel bridges during the 1995 Hyogoken-Nanbu (Kobe, Japan) earthquake—a North American perspective. *Eng Struct*. 1998;20(12):1063-1078.
50. Earthquake Engineering Research Institute. Lorna Prieta earthquake reconnaissance report. Spectra. supplement to vol. 6, Oakland, Calif. 1990.
51. Earthquake Engineering Research Institute. Northridge Earthquake. Jan. 17, 1994, preliminary reconnaissance report. Oakland, Calif. 1994.
52. Calvi GM. Recent experience and innovative approaches in design and assessment of bridges. Proc., 13th World Conference on Earthquake Engineering, Vancouver, Canada; 2004. August 1–6, 2004, Paper No. 5009.
53. Tubaldi E, Dall'Asta A. Transverse free vibrations of continuous bridges with abutment restraint. *Earthq Eng Struct Dyn*. 2012;41(9):1319-1340.
54. Tubaldi E, Dall'Asta A, Dezi L. Reduced formulation for post-elastic seismic response of dual-load path bridges. *Eng Struct*. 2013;51:178-187.
55. Kikuchi M, Nakamura T, Aiken ID. Three-dimensional analysis for square seismic isolation bearings under large shear deformations and high axial loads. *Earthq Eng Struct Dyn*. 2010;39(13):1513-1531.
56. Kikuchi M, Aiken ID. An analytical hysteresis model for elastomeric seismic isolation bearings. *Earthq Eng Struct Dyn*. 1997;26:215-231. doi:10.1002/(SICI)1096-9845(199702)26:2
57. Micozzi F, Flora A, Viggiani LRS, Cardone D, Ragni L, Dall'Asta A. Risk assessment of reinforced concrete buildings with rubber isolation systems designed by the Italian Seismic Code. *J Earthq Eng*. 2021;26:7245-7275. doi:10.1080/13632469.2021.1961937
58. Ponzo FC, Di Cesare A, Telesca A, Pavese A, Furinghetti M. Advanced modelling and risk analysis of RC buildings with sliding isolation systems designed by the Italian Seismic Code. *Applied Sciences*. 2021;11(4):1938. doi:10.3390/app11041938
59. Furinghetti M, Yang T, Calvi PM, Pavese A. Experimental evaluation of extra-stroke displacement capacity for Curved Surface Slider devices. *Soil Dyn Earthq Eng*. 2021;146:106752.
60. Cardone D. Displacement limits and performance displacement profiles in support of direct displacement-based seismic assessment of bridges. *Earthq Eng Struct Dyn*. 2014;43(8):1239-1263.
61. LaFave J, Fahnestock L, Foutch DA, et al. *Experimental Investigation of the Seismic Response of Bridge Bearings*. FHWA-ICT-13-002; 2013.
62. RFI Technical Instruction 44/E. *Istruzione tecnica per il calcolo, l'esecuzione, il collaudo e la posa in opera dei dispositivi di vincolo e dei coprigiuntinegli impalcati ferroviari e nei cavalcavia*. Rete Ferroviaria Italiana; 2002. (In Italian).
63. Cardone D, Viggiani LRS, Perrone G, et al. Modelling and seismic response analysis of existing Italian residential RC buildings retrofitted by seismic isolation. *J Earthq Eng*. 2022;27:1069-1093. doi:10.1080/13632469.2022.2036271
64. Gorini DN, Callisto L, Whittle AJ. An inertial macroelement for bridge abutments. *Geotechnique*. 2022;72(3):247-259. doi:10.1680/jgeot.19.P.397
65. Gorini DN, Callisto L, Whittle AJ, Sessa S. A multiaxial inertial macroelement for bridge abutments. *Int J Numer Anal Methods Geomech*. 2023.
66. Gorini DN, Callisto L. Generalised ultimate loads for piled foundations. *Acta Geotechnica*. 2022;17:2495-2516. doi:10.1007/s11440-021-01386-4
67. Gorini DN, Whittle AJ, Callisto L. Ultimate limit states of bridge abutments. *J Geotech Geoenvironmental Eng*. 2020;146. doi:10.1061/(ASCE)GT.1943-5606.0002283
68. Okabe S. General theory on earth pressure and seismic stability of retaining walls and dams. *J Jpn Soc Civil Eng*. 1924;10(6):1277-1323.
69. Mononobe N, Matsuo O. On the determination of earth pressure during earthquakes. *Proceeding of the World Engineering Congress*. 1929;9:179-187.
70. Gorini DN, Callisto L, Whittle AJ. Dominant responses of bridge abutments. *Soil Dyn Earthq Eng*. 2021;148:106723. doi:10.1016/j.soildyn.2021.106723
71. El Naggar MH, Novak M, Sheta M, El Hifnawi L. DYNA 6: A computer program for calculation of foundation response to dynamic loads. 2011.

72. CALTRANS. Seismic design criteria (version 2). 2019.
73. Franchin P, Pinto PE. Performance-based seismic design of integral abutment bridges. *Bull Earthq Eng*. 2013;12(2):939-960.
74. Marchi A, Gallese D, Gorini DN, Franchin P, Callisto L. On the seismic performance of straight integral abutment bridges: from advanced numerical modelling to a practice-oriented analysis method. *Earthq Eng Struct Dyn*. 2022;52:164-182. doi:10.1002/eqe.3755
75. Vamvatsikos D, Cornell CA. Incremental dynamic analysis. *Earthq Eng Struct Dyn*. 2002;31(3):491-514. doi:10.1002/eqe.141
76. Iervolino I, Baraschino R, Belleri A, et al. Seismic fragility of Italian code-conforming buildings by multi-stripe dynamic analysis of three-dimensional structural models. *J Earthq Eng*. 2023. doi:10.1080/13632469.2023.2167889
77. Iervolino I. Estimation uncertainty for some common seismic fragility curve fitting methods. *Soil Dyn Earthq Eng*. 2022;152:107068.

How to cite this article: Franchin P, Baltzopoulos G, Biondini F, et al. Seismic reliability of Italian code-conforming bridges. *Earthquake Engng Struct Dyn*. 2023;1-24. <https://doi.org/10.1002/eqe.3958>

APPENDIX

FRAGILITY PARAMETERS

TABLE 5 Fragility parameters for all structures and both performance levels. The last two columns report the rate of exceedance of SD.

Bridge/site	Limit state	Frag. method	IM	η	β	Rate of failure (fit)	Rate of failure (RINTC)
TV/AQ	SD	ML	Sa(1.0)	-1.507	0.641	3.12E-03	4.67E-03
	UPD	ML	Sa(1.0)	-1.701	0.565	3.79E-03	4.84E-03
TV/MI	SD	ML	Sa(1.5)	-1.501	0.687	1.11E-05	4.49E-06
	UPD	ML	Sa(1.5)	-1.501	0.687	1.11E-05	1.37E-06
TV/NA	SD	ML	Sa(1.0)	-1.133	0.533	3.77E-04	6.55E-04
	UPD	ML	Sa(1.0)	-1.236	0.519	4.75E-04	5.08E-04
SV/AQ	SD	ML	Sa(3.0)	-1.878	0.919	9.47E-04	1.32E-03
	UPD	ML	Sa(3.0)	-2.083	0.906	1.29E-03	1.39E-03
SV/MI	SD	LSF	Sa(0.5)	-0.441	0.109	8.09E-07	4.88E-12
	UPD	ML	Sa(0.5)	-1.053	0.054	1.28E-05	5.01E-06
SV/NA	SD	ML	Sa(2.0)	0.438	1.619	2.34E-04	6.56E-05
	UPD	ML	Sa(2.0)	0.438	1.619	2.34E-04	3.52E-05
IAB/AQ	SD	ML	Sa(0.5)	0.800	0.308	1.05E-04	1.60E-04
	UPD	ML	Sa(0.5)	0.420	0.297	2.39E-04	2.50E-04
IAB/MI	SD	LSF	Sa(0.5)	-0.004	0.119	8.18E-08	3.83E-29
	UPD	LSF	Sa(0.5)	0.111	0.356	2.00E-07	4.85E-09
IAB/NA	SD	LSF	Sa(0.5)	1.768	0.331	4.16E-08	1.33E-08
	UPD	ML	Sa(0.5)	0.087	0.424	6.54E-05	6.02E-05
TO/NA	SD	ML	Sa(0.5)	0.118	0.491	7.88E-05	1.73E-04
	UPD	ML	Sa(0.5)	-1.348	0.530	3.70E-03	8.25E-03
TO/MI	SD	LSF	Sa(0.5)	-0.112	0.779	2.04E-05	1.91E-05
	UPD	ML	Sa(0.5)	-1.838	0.706	2.08E-03	9.43E-03
FPS/AQ	SD	ML	Sa(2.0)	-1.029	1.033	6.42E-04	4.18E-04
	UPD	ML	Sa(2.0)	-1.029	1.033	6.42E-04	3.95E-04
FPS/NA	SD	ML	Sa(2.0)	0.801	1.292	1.76E-05	1.27E-05
	UPD	ML	Sa(2.0)	-0.167	0.880	1.16E-05	6.06E-06
HDRB/AQ	SD	ML	Sa(1.5)	-0.790	0.237	1.86E-04	1.76E-04
	UPD	ML	Sa(1.5)	-0.790	0.237	1.86E-04	1.60E-04
HDRB/NA	SD	ML	Sa(1.5)	-0.497	0.863	7.32E-05	4.46E-05
	UPD	ML	Sa(1.5)	-0.497	0.863	7.32E-05	2.24E-05